POLITECNICO DI TORINO

Master's Degree in Electric Engineering

Master's Degree Thesis

Real-time grid parameters estimation for stability improvement of ultra-fast charging stations

Supervisors

Prof. Radu BOJOI

Ing. Alessandro ROVERI

Candidate

Giacomo IMPERIALE

Luglio 2024

Abstract

The increasing prevalence of electric vehicles (EVs) requiring Ultra-fast charging (UFC) stations is beginning to create significant challenges for the operation of the electric power system. This thesis aims to analyze, compare, and simulate state-of-the-art solutions for real-time identification of grid parameters. The research involves conducting a comprehensive literature review to identify the most promising solutions, developing and implementing a robust identification algorithm, and evaluating each method in a PLECS simulation environment under various grid conditions. To achieve this, an active front-end (AFE) three-phase AC/DC converter model will be implemented.

The most appropriate estimation methods will be implemented and tested in the field to verify their effectiveness and reliability. A final comparison of the selected methods will be performed under different grid conditions to determine the best approach for various scenarios.

All thesis activities will be conducted in collaboration with the Prima Electro R&D department, leveraging their resources and expertise. This collaboration ensures the practical applicability and robustness of the developed solutions.

Acknowledgements

"HI"

Goofy, Google by Google

Table of Contents

List of Tables

List of Figures

x

Listings

Chapter 1

Introduction

1.1 Forecasts on the growth of grid-tied converters

The increasing prevalence of electric vehicles (EVs) requiring ultra-fast charging (UFC) stations is beginning to create significant challenges for the operation of the electric power system. UFC stations are characterized by high peak power demands and irregular operation, which can affect the stability of the power grid. The amount of grid connected converters has greatly increased in the past few years and according to the most relevant scenario on future trends of renewable energy and battery chargers, the growth will not stop in the next years. The most important publication on recent developments and future trends in electric mobility is the *IEA Global EV Outlook 2024*. [1].

According to this report, the market share of plug-in hybrid electric vehicles (PHEVs) and electric vehicles (EVs) has been steadily increasing, especially driven by significant growth in the Chinese market. In Europe, there is a consistent upward trend in electric vehicle sales, with countries in Northern Europe leading

the way. It can be seen in Fig. 1.1,
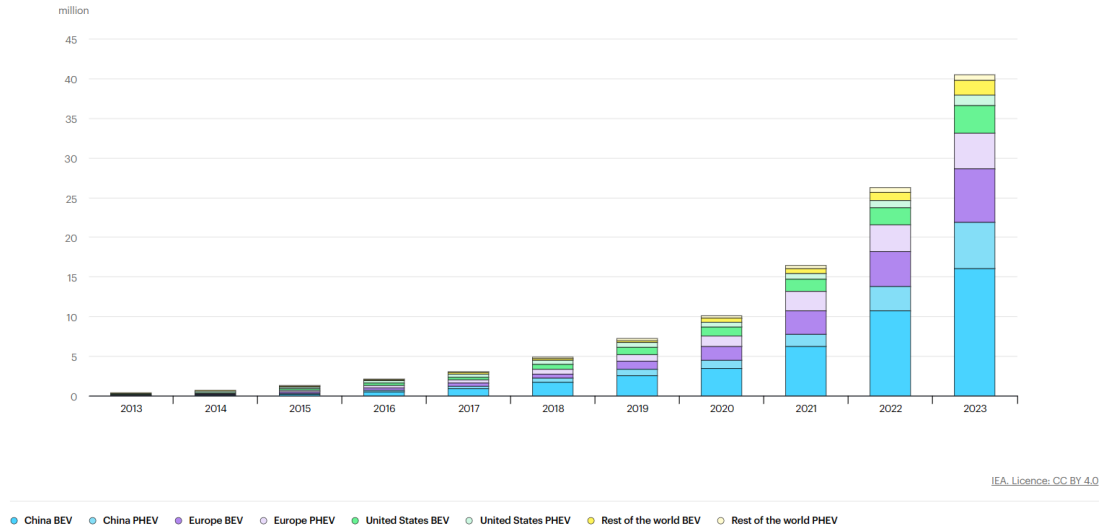
Figure 1.1: Market share of PHEVs and EVs in recent years. Source: [1]

In 2023, there were more than 250,000 new vehicle registrations weekly, a figure exceeding the total annual registrations in 2013, a decade earlier. electric vehicles constituted approximately 18% of total vehicle sales in 2023, marking an increase from 14% in 2022 and a significant rise from 2% recorded five years prior, in 2018. These patterns indicate a sustained growth as the electric vehicle market continues to mature. Battery electric vehicles represented 70% of the electric vehicle inventory in 2023.

It is important to take a look on future trends, analysing *STEPS*(Socio-Technical Energy Transition Pathways), which refers to scenarios of socio-technical energy transition. As shown in Fig. 1.2 the stock of EVs grows from less than 45 million in 2023 to 250 million in 2030 and reaches 525 million in 2035. As a result, in 2035, more than one in four vehicles on the road is electric. On average, the EV stock grows by 23% annually from 2023 to 2035.

The growth trends of the electric vehicles (EVs) stock are intrinsically linked

million vehicles

● PLDVs - BEV   ● PLDVs - PHEV   ● LCVs - BEV   ● LCVs - PHEV   ● Buses - BEV   ● Buses - PHEV   ● Trucks - BEV   ● Trucks - PHEV
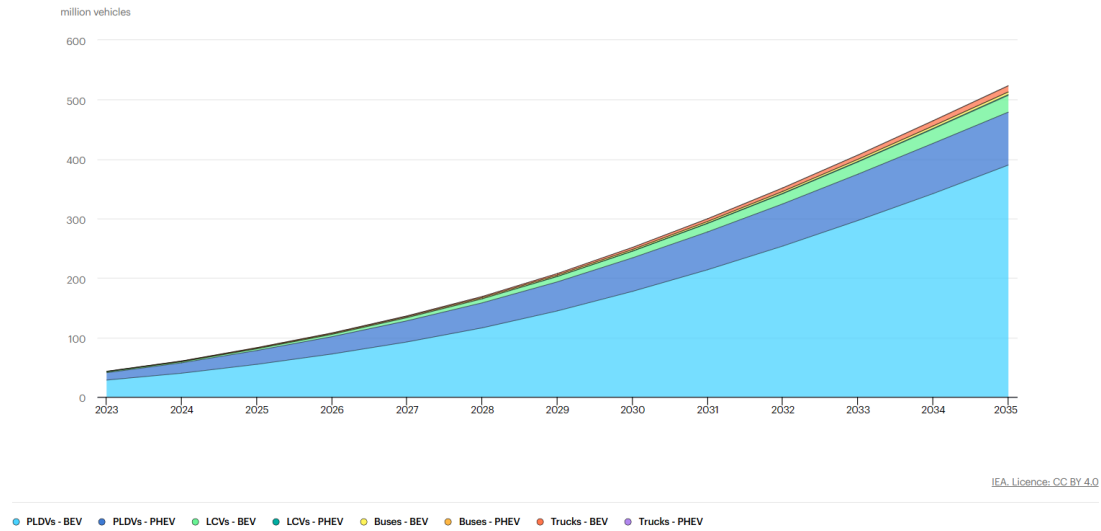
Figure 1.2: Electric vehicle stock by mode in the Stated Policies Scenario, 2023-2035. Source: [1]

to the expansion trends of charging infrastructure. Thanks to [1] it is possible to analyse them too. Home charging is the preferred method for EV owners, especially in regions with higher voltage grids like Europe and Australia, where overnight charging from a regular domestic socket is common. Access to home charging varies significantly across regions due to differences in urban density and income levels. In densely populated cities like those in Korea, public charging is more relied upon. In lower voltage regions such as the United States and Canada, dedicated chargers are necessary for efficient overnight charging. Beyond home charging, private non-publicly accessible chargers are also significant, with many located in workplaces and fleet facilities. Overall, the amount of public chargers is higher than home charging stations.

As illustrated by Fig 1.3, the difference between the public and private chargers is relevant, but it is also important to notice the robust upward trend of installed chargers.
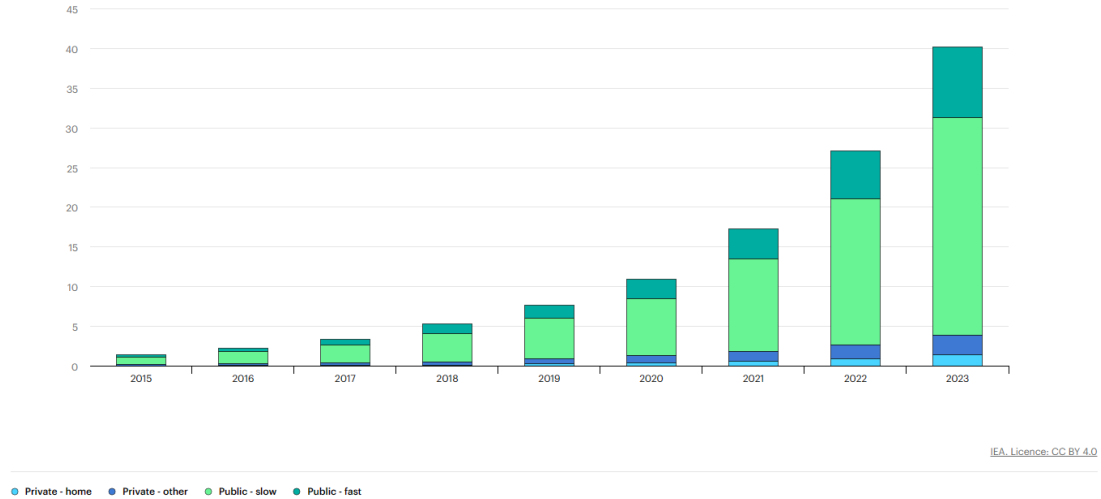
Figure 1.3: Public and private installed light-duty vehicle charging points by power rating and by type, 2015-2023. Source: [1]

It is also necessary to analyse the outlook for the next years, in order to thoroughly understand the possible scenarios and the future challenges to deal with.

Thanks to 1.4 we can analyse the trends with two different scenarios. The global count of home chargers in 2023 amounted to approximately 27 million, with a charging capacity of 150 GW and an average of 1.6 electric LDVs per charger. By 2035, this figure is projected to exceed 270 million in the STEPS scenario and approximately 300 million in the APS scenario. The stock of private chargers, including home and other private chargers, is anticipated to increase up to 14-fold by 2035 in the APS, while public chargers are expected to experience a sixfold increase. Despite access to home charging, EV owners still utilize public charging to some degree, with the share of charging from non-home chargers projected to
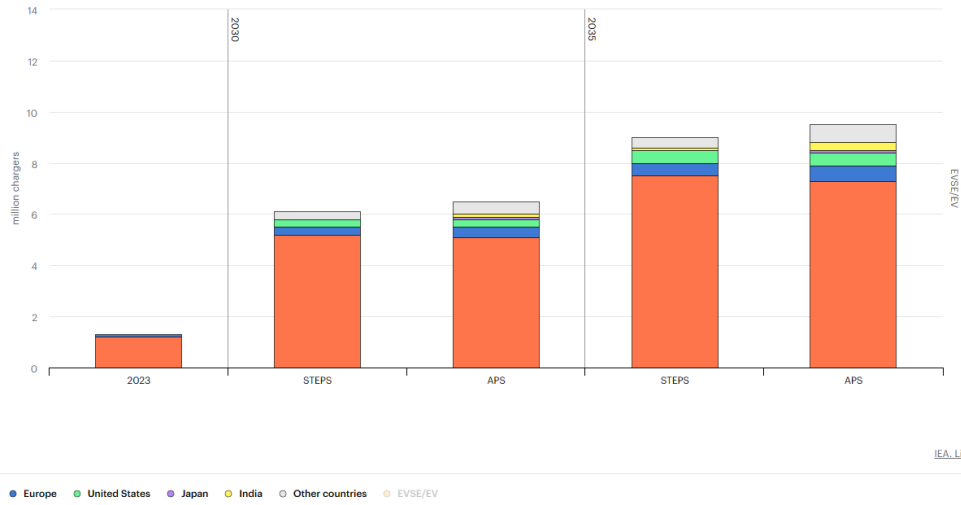
Figure 1.4: Number of public light-duty vehicle fast chargers installed by region, 2023-2035. Source: [1]

rise to nearly 45% by 2035, compared to less than 35% in 2023.

Looking at all these forecasts, it is clear that the following decades will see a great increase in grid connected converters, bringing to many well-known technical and economical issues and challenges. In particular, the increasing number of converter connected to the grid is linked to the problem of variability of network impedance. In the next sections, there will be presented some methods that can be useful for addressing those issues.

1.2   Thesis objectives

The goals of this thesis are to analyze, compare, and simulate state-of-the-art solutions for real-time identification of grid parameters. This involves conducting a comprehensive literature review to identify the most promising solutions, developing and implementing a robust identification algorithm, and evaluating each method in *PLECS* simulation environment under various grid conditions. To do so, it has been decided to implement a converter model and in particular, an active front-end (AFE) three-phase AC/DC converter. An analytical study of the interaction between the grid-tied inverter filter and the grid will also be conducted. The most appropriate estimation methods will be implemented and tested in the field to verify its effectiveness and reliability. A final comparison of the chosen methods will be made under different grid conditions to determine the best method for varying scenarios. All thesis activities will be carried out in collaboration with the Prima Electro R&D department, leveraging their resources and expertise.

1.3   Practical uses of local estimation techniques

Interest in impedance estimation techniques is growing, as grid converters percentage is growing up on the network. It is evident that knowing the value of the network impedance can be helpful in mitigating network instability issues. In this section it will be firstly discussed how estimation techniques can be useful for practical uses. All these arguments are largely discussed in [2].

1.3.1   Network characterisation

The primary focus in network characterization revolves around capturing a broad frequency spectrum and temporal fluctuations within the power network. This enables assessments of power quality and informs decisions regarding protection and filtering designs. Referring to [3] the quality of the electrical power delivered to local users has suffered deterioration over recent years because of the increasing use of nonlinear loads (NLLs)—usually power-electronic systems. To mitigate harmonic distortion, methods like passive filtering and active filtering are employed, to absorb local harmonic currents and prevent their propagation into the main power supply network. Designing an effective passive filter necessitates a thorough understanding of the supply impedance and its fluctuations over time to avoid creating resonance conditions, which could potentially destabilize the power system. Active filters also require a comprehensive understanding of the system impedance to ensure stable controller operation and can even assist in generating the reference currents for the filter. Alternatively, knowledge of the impedance characteristics of a specific installation could be leveraged to redistribute non-linear loads (NLLs) within the installation, thereby mitigating power quality degradation at critical points within the network.

1.3.2   Anti-Islanding detection

An islanding scenario occurs when a segment of the grid is powered exclusively by local Distributed Energy Resources (DERs) via their associated Point of Common Coupling (PCC), while being electrically isolated from the broader power system. Fig. 1.5 There are two types of islanding operation: intentional and non-intentional. The last situation is prohibited for DERs connected on the meter side as per IEEE 1547 regulations. Hence, these DERs must promptly detect islanding and discontinue supplying power to the local load within 2 seconds of the island forming. Various techniques exist for detecting islanding, with one method leveraging local impedance estimation. Essentially, if the calculated impedance significantly deviates from its previous value by a predetermined threshold set by the system operator (e.g., 1 Ω), the monitoring system will infer that the converter is operating in island mode and adjust its reference operations accordingly. [4].
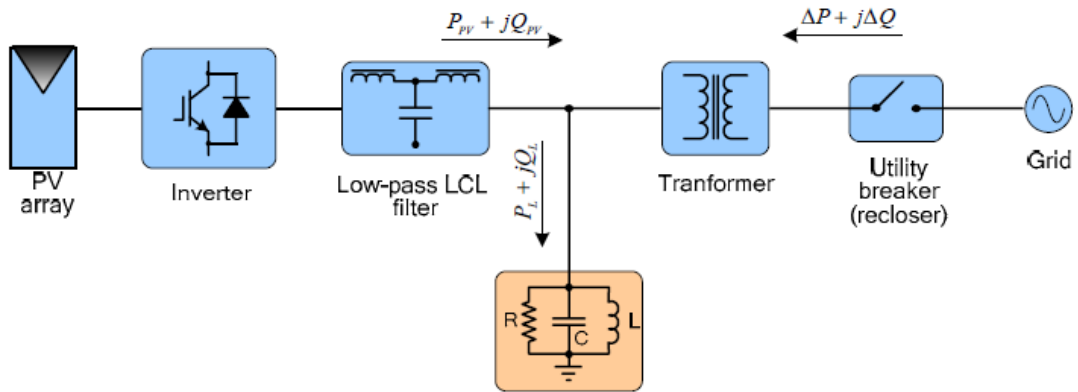
Figure 1.5: Islanding operation phenomenon: [5]

1.3.3   Adaptive control of converters

The grid impedance (Z_{grid}) significantly influences the current control of grid converters, requiring adaptation to substantial variations. The grid impedance parameters are crucial for the safe operation of a grid-connected converter. The performance of the converter relies on the grid impedance (Z_{grid}) and the voltage at the Point of Common Coupling (V_{PCC}), which is often highly distorted due to other nonlinear loads connected to the PCC. The current controller, which regulates the current to the grid, is designed based on the converter's output filter impedance (Z_{conv}) and an assumed value of the grid impedance (Z_{grid}). The stability of these controllers depends on the grid impedance, as it adds serially to the converter's output filter. With the increasing penetration of distributed power generation systems, the grid impedance at various points of common coupling can vary significantly, mainly due to grid interface filters. This substantial variation in grid impedance reduces the robustness of the current controller and can lead to instability. When the grid impedance is unknown, designing the current controller involves a trade-off between performance and stability. Selecting controller parameters with a specific stability margin results in poor performance when the actual grid impedance differs from the design assumptions. Therefore, the stability threshold can be easily reached or exceeded with realistic variations in grid impedance or sudden changes in grid impedance. Consequently, variations in grid impedance are a problem both for the safety and stability of the current controller and its performance. By detecting the grid impedance online, the current controller can be adjusted in real-time, ensuring that the controller parameters align with the actual grid impedance. Fig. 1.6 can be useful to undestand this method. This adjustment maintains both stability and optimal performance, regardless of the grid impedance value. [6]
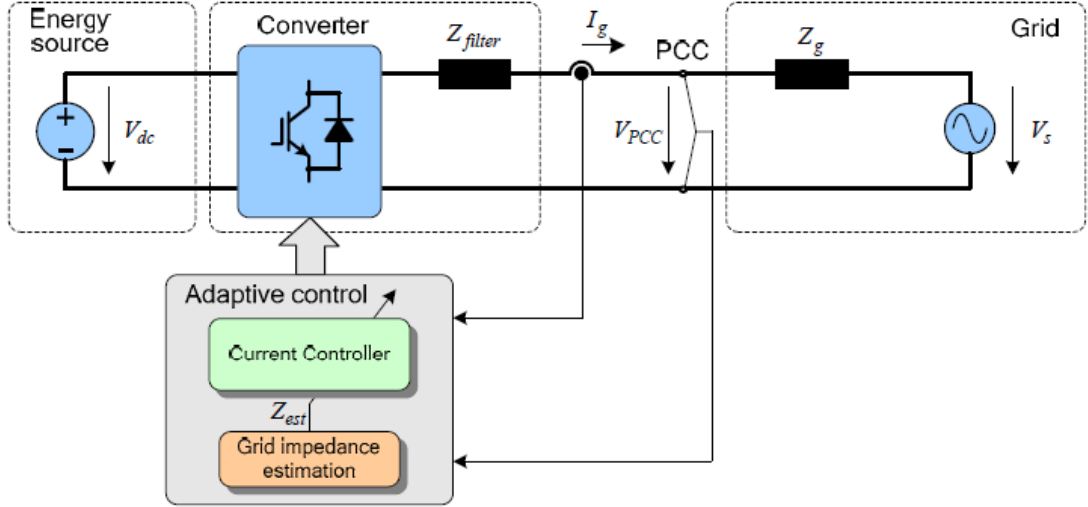
Figure 1.6: Adaptive control scheme for grid-connected converter: [5]

1.3.4   LCL filter resonance avoidance

To ensure stable operation and avoid resonance issues in grid-connected converters with LCL filters, accurate impedance estimation and dynamic control adjustment are critical. LCL filters, composed of two inductors (L_1 and L_2) and a capacitor (C), are effective at attenuating high-frequency harmonics. However, they introduce a resonance frequency (f_{res}) that can destabilize the system if not properly managed. The resonance frequency is given by:

$$f_{\text{res}} = \frac{1}{2\pi}\sqrt{\frac{L_1 + L_2}{L_1 L_2 C}}$$

Variations in grid impedance (Z_{grid}) can shift the resonance frequency, potentially leading to instability. Accurate, real-time estimation of grid impedance can be useful for adaptive control strategies that can mitigate these effects. If the estimated impedance indicates a shift in the resonance frequency, control parameters can be modified to account for this shift. This may involve tuning the filter parameters or adjusting the control gains to maintain stability. Active damping can be

implemented to counteract resonance. This involves modifying the control algorithm to introduce damping at the resonance frequency.

1.4 Classification of local impedance estimation techniques

Thanks to the previous section, it is clear that the grid impedance Z_{grid} is an important grid parameter that needs to be evaluated with accuracy, and in case of real-time issues it needs to be calculated quickly. For this reason, in the literature there are so many methods for the estimation, and for each method there is a specific purpose, but also differences in terms of performances. It can be useful to classify each method, as can be seen in [2]. Estimation techniques can be categorized into active, passive, or quasi-passive methods, based on whether the perturbation is deliberately and periodically introduced, naturally occurring in the grid, or initiated by an observer to activate an estimation method. The techniques analysed in this thesis are all applied in converters, as depicted in Fig. 1.7. In this figure, V represents the converter voltage, I_c is the converter current, R_c, L_c, and C_f denote the resistance, inductance, and capacitance of the converter filter, respectively. The PCC voltage is represented by U, the grid resistance by R_n, the grid inductance by L_n, and the grid voltage by E_n. These techniques often treat the network impedance as an aggregated impedance, either considered linear and represented by its Thévenin equivalent (with R_n and L_n being constant), or as nonlinear (where $R_n(\omega)$ and $L_n(\omega)$ vary with frequency).
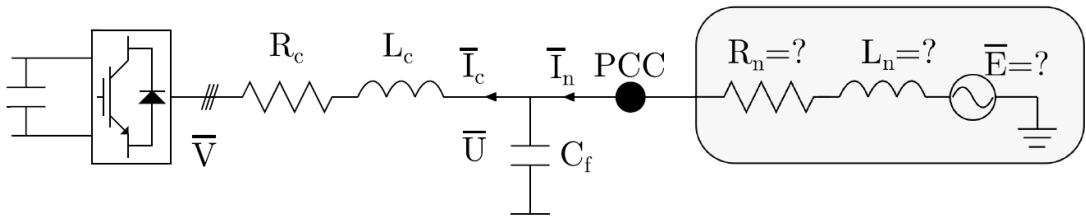
Figure 1.7: Converter connected to PCC, with unknown Thévenin equivalent impedance and equivalent grid voltage. Source: [2]

1.4.1 Passive techniques

Passive techniques utilise existing transients, caused by sufficiently large grid events, to undertake impedance estimations. Passive techniques can be subdivided in:

- Local PMU derived observers

- PCC observers

- Kalman Filters

Passive methods relies on the non-characteristic signals (line voltages and currents) that are already present in the system. This approach depends on the existing background distortion of the voltage. However, in many instances, the distortion does not have sufficient amplitude or repetition rate to be accurately measured. For this reason, and keeping in mind that accuracy and rapidity of estimation are mandatory, the passive methods are not suitable for our purpose [7][8][9][10].

1.4.2 Active techniques

Active techniques differs from passive techniques, in fact they do not depend on existing grid events. Instead, these methods deliberately introduce a controlled disturbance or alter the operating point to enhance the amount of information obtainable from the network. The disturbance consists in variations in the power supply network, which is followed by data acquisition and signal processing. The manner of "disturbing" the network can differ, leading to the categorization of active methods into two main types. [5]

Transient methods

Transient methods are particularly advantageous for quickly obtaining results, as the perturbation effect on the network has a limited, short time. With this technique, an impedance measuring device rapidly introduces a transient current into the network (such as a resistive short circuit), then measures the grid voltage and current at two distinct time points—before and after the transient event. The transient impulse induces a broad harmonic spectrum that requires subsequent analysis. The results acquired provide insight into the network's response across a wide frequency range, making this method suitable for applications requiring impedance characterization at various frequencies. However, implementing this method may necessitate high-performance A/D acquisition devices and the use of specialized numerical techniques to mitigate noise and random errors. These requirements are challenging. It means that a good and strong processor is needed. The computational capability in converters is not always so high, and for that reason this type of techniques is not suitable for our purpose.

Steady-state methods

Steady-state methods usually introduce a known periodic distortion into the grid and subsequently conduct analyses during the steady-state period. This type of techniques necessitate that the network response to a disturbance stabilizes before any measurements are taken. In addition, these techniques operate under the assumption of consistent network conditions throughout the testing period. In the literature, different methodologies can be found:

- Frequency sweeps

- Non-harmonic excitation

- P/Q reference variations

This kind of techniques are easier to implement on *C-script* and requires a low computational capability. In addition, thanks to [2] their performance in accuracy and rapidity are quite good, and for that reason they are suitable for our purpose. In the next sections, some of those methods will be chosen, analysed and implemented.

1.4.3   Quasi-Passive techniques

Quasi-passive techniques combine an observer with an active technique. The observer is utilized to identify changes in the network impedance. If a change is detected, the active technique is triggered. This approach can be seen as balance between maximizing estimation quality and minimizing disturbance injection. By monitoring grid changes, a predetermined criterion can initiate the active technique, introducing a disturbance only when necessary. For example, the trigger can be a "quality threshold" Γ, that can be calculated:

$$\Gamma_k = \frac{1}{2k} \sum_{i=k-n}^{k+n} \frac{|\, V_i - I_{ni} \cdot \hat{Z}_{ni} - \hat{E}_i\,|^2}{|I_{ni}|}$$

In which, there are voltage and current measured (V_i and I_{ni}) and estimated Impedance and Grid voltage ($\hat{Z}_{ni}, \hat{E}_i$). Ideally, when the estimation values are accurate, the quality threshold should be close to zero. However, quasi-passive techniques introduce additional delays due to the time required for the observer to detect impedance changes. This approach can be a easy way to estimate the parameters with an high accuracy and with low disturbances, but will not be analysed in this study. [11][12]

Chapter 2

Grid and converter model

Following the technical literature review, the initial step involved the development of a grid converter model. To accomplish this task, the *PLECS* simulation environment was employed. This is needed in order to facilitate simulation of measurements and validate the data processing scripts before practical experimentation in the laboratory.

In the development process, the control structure and the development and implementation of the control scheme has been carried out.

2.1   System structure

In 1.2 it has been presented the model that will be implemented. In 1.7 it can be seen a preliminary scheme of the Ultra-fast charging station. It is composed of two main stages. The first stage is called AFE (Active-Front-End), directly connected to the grid. In particular, it is a grid-connected three-phase AC/DC converter, connected to the grid through a LCL input filter. The second stage is a DC/DC converter which connects to the load, but it is beyond the scope of this thesis. The focus is on the first stage. A three-phase inverter is a crucial component in

energy conversion systems, particularly relevant for applications in micro-grids and renewable energy systems. Its ability to convert energy between direct current (DC) and alternating current (AC) in both directions allows for greater operational flexibility. This section focuses on the detailed modeling of a three-phase inverter connected to the grid, which includes an LCL filter for harmonic reduction, a point of common coupling (PCC), and a DC link representing the load. [13]
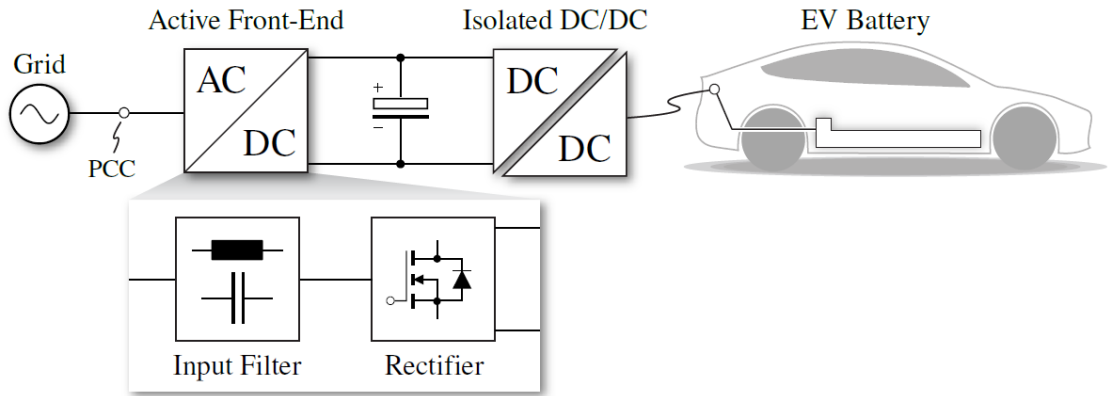
Figure 2.1: Block Diagram of an Ultra-Fast charging station [13]

2.1.1 Active Front-End model
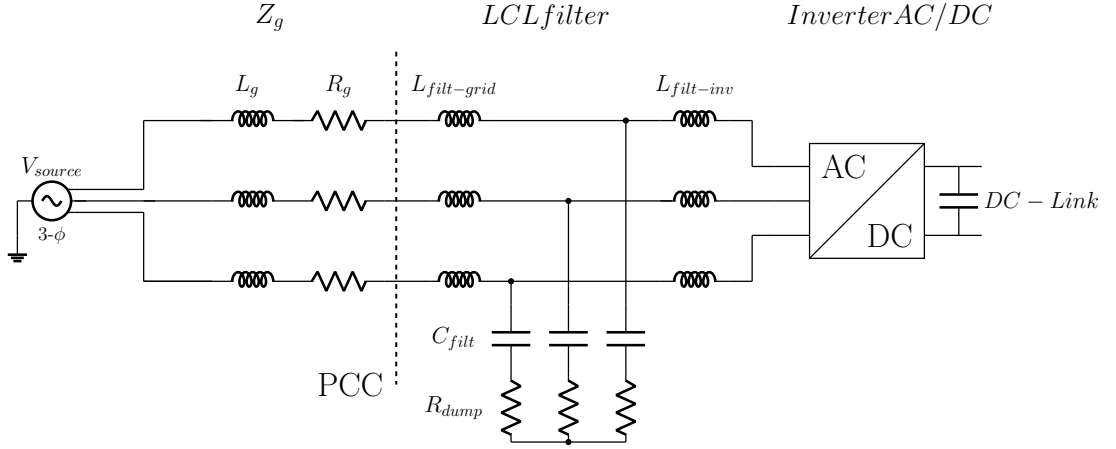
Figure 2.2: Block Diagram of Grid model including AFE, LCL filter and Dc-Link

Thanks to 2.2 it can be seen the structure of the model. It is composed of:

- **Grid model**: Three-phase generator model, and the blocks for grid impedance Z_g in particular R_g and L_g.

- **LCL input filter**: Typical input filter model with grid side inductance $L_{filt-grid}$, inverter-side inductance $L_{filt-inv}$, capacitors C_{filt} and dumping resistances R_{dump}.

- **PCC**: The point of common coupling, where the system connects to the grid and in which all the grid measurements are taken.

- **Inverter**: Three-phase AC/DC inverter connected to DC -Link(load).

2.1.2   Grid model

The grid model represents the three-phase electrical network to which the bidirectional inverter is connected. The model incorporates key parameters such as line impedance, grid voltage, and frequency, which are crucial for accurate simulation and control.

Table 2.1: Essential parameters of the grid model

Parameter	Value	Unit
Grid Voltage (V_{grid})	400	V (line-to-line RMS)
Grid Frequency (f_{grid})	50	Hz

The grid voltage (V_{grid}) is set at 400 V RMS (line-to-line), which is typical for medium-voltage distribution systems. The grid frequency (f_{grid}) is 50 Hz, in line with standard power systems in many regions. The line impedance (Z_{line}) reflects the resistive and inductive properties of the transmission line. Network impedance is a fundamental measure to characterize the behavior of an electrical system under various operating conditions. It is expressed in complex form as:

$$\hat{Z} = R + jX \tag{2.1}$$

where R represents the resistance (real component) and X the reactance (imaginary component). Network impedance can vary depending on the system configuration and load conditions. The complex representation allows for visualization of impedance in the complex plane, facilitating the analysis of its properties.

In the complex plane, the real component (horizontal axis) and the imaginary component (vertical axis) can be positive or negative, indicating different network characteristics. In fact, the impedance can be more resistive or more inductive depending on the grid components.

Graphical visualization of these properties is crucial for understanding the

dynamic behavior of the electrical network.
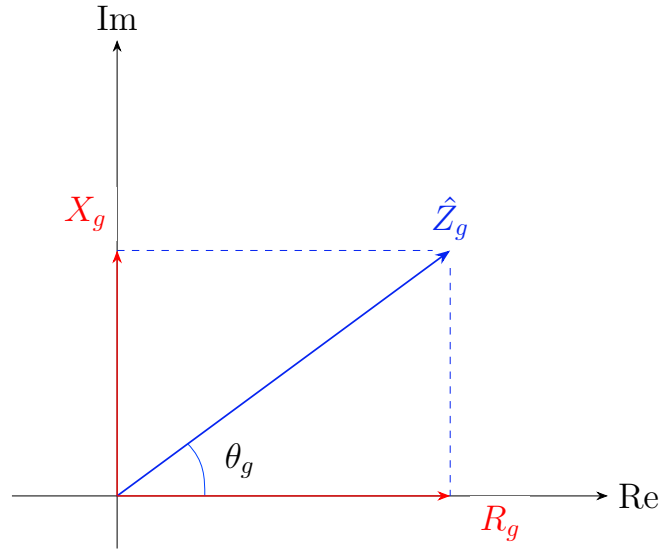
Figure 2.3: Representation of network impedance in the complex plane.

By incorporating these parameters, the grid model enables a comprehensive analysis of the inverter-grid interaction, ensuring the system's performance and stability under various operating conditions.

2.1.3 LCL input filter

The input filter of the Active Front End (AFE) ensures compliance with grid current harmonic restrictions at the Point of Common Coupling (PCC), according to standards such as IEEE 519 [14]. The filter's primary function is to attenuate high-frequency harmonics generated by the converter's Pulse-Width Modulation (PWM) operation, preventing them from entering the grid and affecting other devices connected to the PCC.

An LCL filter offers superior performance due to its high attenuation capability (up to 60 dB/dec roll-off), resulting in reduced filter size and losses. However, the higher order of the LCL filter introduces design complexity, with multiple degrees

of freedom and various constraints to consider. Additionally, filter resonance can amplify unwanted harmonics and negatively impact the closed-loop current control, potentially leading to instability. Mitigation of the resonance peak requires passive or active damping methods, maybe using grid impedance estimation [13].

In particular, for this model, an LCL filter with dumping resistor has been chosen. The parameters are selected from already existing components. The following table presents the essential parameters of the LCL filter, including the grid-side inductance, inverter-side inductance, capacitors, and damping resistance.

Table 2.2: LCL filter parameters

Parameter	Symbol	Value
Grid-side Inductance	L_{fg}	200 μH
Inverter-side Inductance	L_{fi}	200 μH
Filter Capacitance	C_f	6 μF
Damping Resistance	R_d	10 Ω

The grid-side inductance (L_{fg}) and inverter-side inductance (L_{fi}) are chosen to balance the trade-off between filtering performance and cost. The filter capacitance (C_f) determines the filter's resonant frequency and its ability to attenuate high-frequency harmonics. The damping resistance (R_d) is selected to mitigate the resonance peak, ensuring stability and effective harmonic attenuation. [15]

2.1.4 Inverter structure and DC-Link

For this thesis, it is not important to specify the inverter model and the switches type. Hence, a Power model composed of a 3-phase 2-level VSI with ideal IGBT switches has been chosen. All the switches are controlled with their input modulation signals q_x, which are the final output of the control block of the model. It can be seen in 2.4.
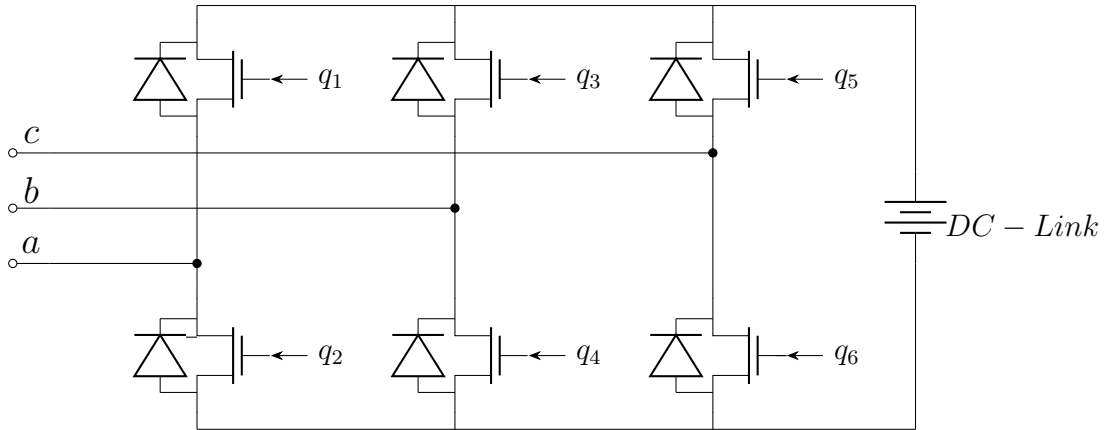
Figure 2.4: Inverter and DC-Link model

To end with, the DC-link acts as an interface between the inverter and the load. It is typically modeled as a capacitor that stores energy and provides a buffer for power fluctuations. Maintaining a stable voltage level in the DC link is crucial for efficient system operation. In this case, also the DC-Link is ideal, modeled has a battery connected directly to the DC side of the inverter.

In particular, $V_{dc} = 800$ V.

2.2   Inverter control scheme

Converters operate in various modes to meet different application requirements. In particular, this model can be seen as Grid-Following/Feeding converter. As a battery charger, it needs to absorb Active and Reactive power from the grid in order to inject it through the load. Grid-following converters are designed to synchronize with the grid voltage and follow its frequency and phase. They operate by adjusting their output to match the grid conditions, ensuring that the converter remains in phase with the grid. This mode is particularly important for applications such as renewable energy systems, where the power generated needs to be injected into the grid in a controlled and synchronized manner. The operation of this type of converters involves continuously monitoring the grid voltage and using control algorithms to maintain synchronization. This is achieved through phase-locked loops (PLLs) that track the grid's frequency and phase, adjusting the converter's output accordingly. In 2.5 it can be seen a preliminary control scheme. It starts from the P^* and Q^* reference frame, which are the desired values of Active and Reactive power and taken as an input. The GFL control purpose is to transform the P/Q references in current references, and after the current control loop, the input modulation signals q_x are generated. [15]
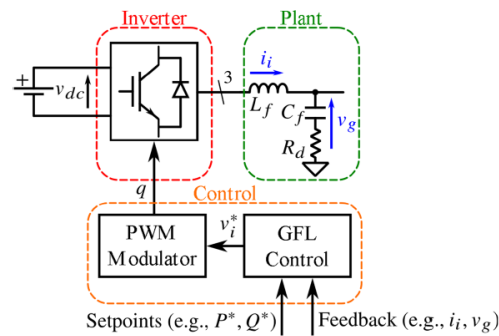
Figure 2.5: Grid-Following converter control scheme [15]
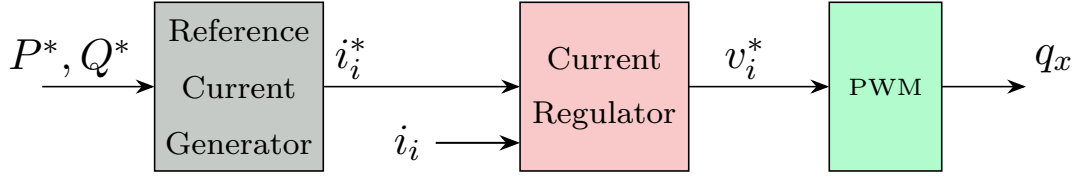
Figure 2.6: Block diagram control scheme with P/Q references [15]

In 2.6 it can be seen that the GFL control is composed of a Reference Current Generator, the Current Regulator and the signal modulation.

It is important to notice that the Grid-Following converter has a voltage oriented control. In particular, we need a *dq* rotating reference, which can be defined with the measurements on the PCC (Point of Common Coupling), in order to get the synchronisation of the converter to the grid. In addition, the *dq* rotating reference is useful for the PQ reference frame. In fact it is used in the Akagi theory for decomposing power components in electrical systems. The Akagi theory, also known as the instantaneous power theory, transforms three-phase quantities into the *dq* reference frame using the Park transformation. This transformation facilitates the separation of the instantaneous active and reactive power components, providing a robust framework for power quality analysis and control.

In particular, the d-axis is defined as the active power axis, and the q-axis, which is in quadrature, is the reactive power axis. For this reason, the voltage vector V is aligned with the d-axis. Thanks to this convention,i_d controls the Active power and i_q controls the Reactive power. In Fig. 2.7, it can be seen the $\alpha\beta$ axis and the *dq* rotating frame with the angle θ. For a more accurate explanation of the Clarke transformations and the Rotation matrix we can refer to B.
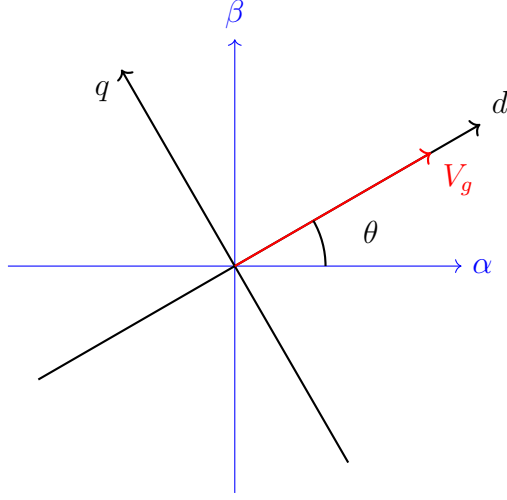
Figure 2.7: *dq* and $\alpha\beta$ axes with voltage V aligned with the *d* axis and angle θ.

2.2.1 P/Q reference current generator

In a grid-following converter, the reference currents are derived from the active and reactive power references to ensure the converter tracks the grid voltage and maintains the desired power exchange with the grid. Utilizing the Akagi theory, we can transform the power references into current references in the *dq* reference frame. The active power P and reactive power Q in the *dq* frame are given by:

$$
\begin{aligned}
P &= v_d i_d + v_q i_q \\
Q &= v_q i_d - v_d i_q
\end{aligned}
\tag{2.2}
$$

To derive the current references i_d^* and i_q^*, we solve the above equations for i_d and i_q:

$$
\begin{aligned}
i_d^* &= \frac{v_{gd}P^* + v_{gq}Q^*}{v_{gd}^2 + v_{gq}^2} \\
i_q^* &= \frac{v_{gq}P^* - v_{gd}Q^*}{v_{gd}^2 + v_{gq}^2}
\end{aligned}
\tag{2.3}
$$

These equations provide the direct and quadrature current references i_d^* and

i_q^* based on the desired active and reactive power P^* and Q^*, as well as the grid voltage components v_{gd} and v_{gq}. By controlling the converter to follow these current references, the desired power exchange with the grid can be achieved, ensuring that the converter operates efficiently and maintains power quality. [15]

2.2.2 Grid synchronization unit, SOGI-PLL

As it has been said previously, in order to get a *dq* frame, the frequency and angle of the grid is needed. It can be extracted from the measurements of current and voltage of the grid on PCC. The quality of grid synchronization directly impacts control performance. An error in phase angle estimation results in incorrect output voltage, leading to errors in power flow or output current relative to the reference. Therefore, the grid synchronization unit must be robust and thoroughly tested under various grid conditions to ensure reliable operation, even with some grid voltage distortion. Grid voltage distortions can arise from several factors, including harmonic currents, load switching, adverse weather conditions, and load-break switches. According to IEEE 1159, such events can cause transients, voltage variations, unbalances, distortions, and frequency fluctuations. Hence, grid variables like voltage amplitude and frequency must be continuously monitored, as they cannot be assumed constant in the control process.

There are some algorithms that are used for this purpose. For this model, a robust algorithm has been chosen. The SOGI-PLL, which is based on a combination of the SRF-PLL and the SOGI-filter.

The SRF-PLL is able to track the estimated voltage angle starting from a stationary reference frame $V_{\alpha\beta}$. 2.8. In order to have a robust algorithm which is not influenced by fluctuations and unbalanced voltages, the $V_{\alpha\beta}$ are filtered with the SOGI-filter. A SOGI-filter (Second Order Generalized Integrator) is a resonant filter able to eliminate the negative and harmonic sequence in the measured voltage.
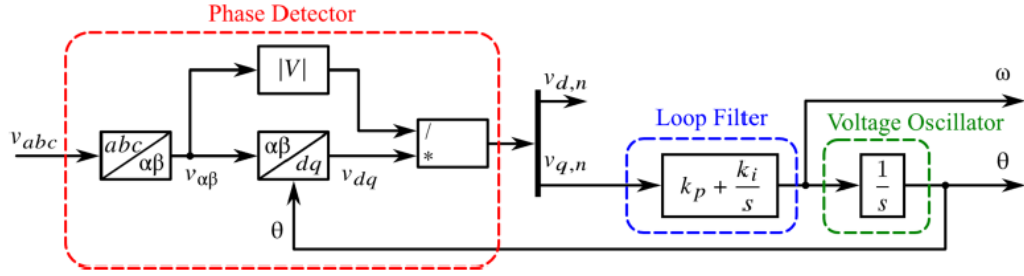
Figure 2.8: Phase Locked Loop for synchronisation to the grid[15]

Thanks to this, the output is the grid voltage at the foundamental frequency with no distortions. 2.9 [15]
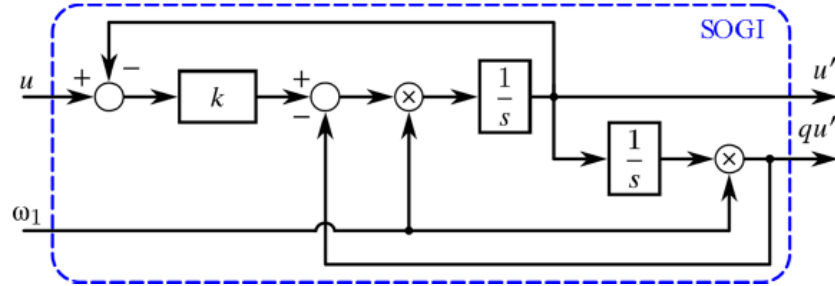
Figure 2.9: SOGI resonant filter [15]

2.2.3 Current control loop

The current control scheme is the same for all the operation modes. In particular, given a reference current i_{in}^* to exchange with the grid (injected or absorbed), the current regulator is able to cancel the error between i_{in}^* and the measured current i_{in}. To do so, the current regulator has the v_{in}^* as output, which applied to the PWM modulator is able to retrieve the inverter signal commands q_x.

The current control is implemented in the *dq* rotating frame, synchronous with the grid voltage vector. This is important because, thanks to this approach, it is possible to cancel the steady state error on the reference current through a

proportional-integral controller. In particular, the *dq* rotating frame is able to make all the controlled variables as continuous quantities. That's because the rotating frame is rotating at the grid frequency ω. However, it must be noted that with a sinusoidal reference a null steady state error can still be obtained by using a P-Res resonant controller, tuned on the frequency of the sinusoidal reference.

Proportional-Integral PI controller

A Proportional-Integral (PI) controller is a control feedback mechanism widely used in industrial control systems. [15] It combines proportional control and integral control to provide a balance between the speed of response and the elimination of steady-state error. The transfer function $H_{PI}(s)$ of the PI controller is given by:

$$H_{PI}(s) = K_p + \frac{K_i}{s}$$

where:

- K_p is the proportional gain, which determines the reaction to the current error.

- K_i is the integral gain, which determines the reaction based on the accumulation of past errors.

In order to tune the PI controller parameters, there are a lot of methods and several key rules of thumb on the literature to consider:

- **Bandwidth frequency** (ω_{bw} [rad/s]: Frequency at which the amplitude of the open-loop transfer function is $\frac{1}{\sqrt{2}}$ (-3 dB). A higher ω_{bw} leads to a faster system response to reference variations. However, it also results in higher sensitivity to high-frequency noises, such as measurement noise.

- **Crossover frequency** (ω_c in rad/s: Frequency at which the amplitude of the open-loop transfer function is 1 (0 dB).

- A typical practice during tuning is to approximate the bandwidth frequency ω_{bw} to the crossover frequency ω_c, so $\omega_{bw} \approx \omega_c$.

In this case, the parameters has been settled in this way:

$$\omega_c = f_c \times 2\pi \tag{2.4}$$

$$K_p = \omega_c \times L_f \tag{2.5}$$

$$K_i = \frac{\omega_c \times K_p}{10} \tag{2.6}$$

2.2.4 Complete control scheme of the grid

It is now possible to get the complete block scheme of the current controller. Firstly, the equations of the plant in the Laplace domain and *dq* frame are needed.

The network equations in the *abc* reference frame describe the three-phase voltages and currents in terms of their respective components. These equations are often represented as follows:

$$v_a = Ri_a + L_f\frac{di_a}{dt} + e_a$$
$$v_b = Ri_b + L_f\frac{di_b}{dt} + e_b \qquad (2.7)$$
$$v_c = Ri_c + L_f\frac{di_c}{dt} + e_c$$

To simplify the analysis, these equations can be transformed into the $\alpha\beta$ reference frame using the Clarke transformation. In the $\alpha\beta$ frame, the network equations become:

$$v_\alpha = Ri_\alpha + L_f\frac{di_\alpha}{dt} + e_\alpha$$
$$v_\beta = Ri_\beta + L_f\frac{di_\beta}{dt} + e_\beta \qquad (2.8)$$

Further simplification can be achieved by transforming these equations into the *dq* reference frame using the Park transformation, which rotates the $\alpha\beta$ frame to align with the rotating reference frame of the voltage or current vector:

$$v_d = Ri_d + L\frac{di_d}{dt} - \omega L_f i_q + e_d$$
$$v_q = Ri_q + L\frac{di_q}{dt} + \omega L_f i_d + e_q \qquad (2.9)$$

The voltage equations in the *d-q* reference frame, transformed into the Laplace domain, are given by:

$$V_d(s) = RI_d(s) + sL_fI_d(s) - \omega L_fI_q(s) + E_d(s)$$
$$V_q(s) = RI_q(s) + sL_fI_q(s) + \omega L_fI_d(s) + E_q(s)$$

$$(2.10)$$

Here, ω is the angular velocity of the rotating reference frame, and the terms $-\omega L_f i_q$ and $\omega L_f i_d$ represent the motional EMF components that arise due to the rotation of the reference frame. This is also defined as cross-coupling phenomenon bewteen d-axis and q-axis. [15]

Finally, the complete diagram can be implemented. 2.10
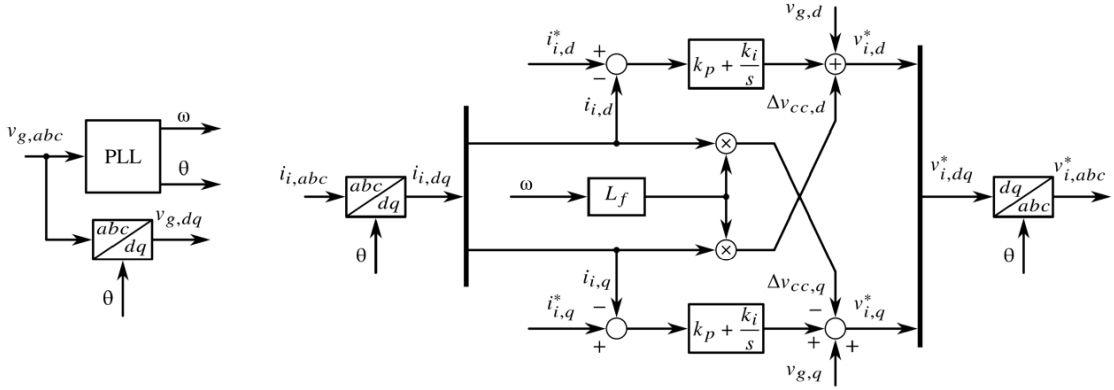
Figure 2.10: Current Control block diagram [15]

It is important to notice that:

- R is neglected.

- The cross-coupling terms can be cancelled by adding (or subtracting) them to the regulator output

- V_g is the feedforward element.

- The PLL tracks θ and ω which are used in the control scheme also for the Clarke transformations.

31

2.2.5 Sinusoidal Pulse Width Modulation S-PWM

Sinusoidal Pulse Width Modulation (S-PWM) is a technique used to control the average power delivered to an electrical load by modulating the width of the pulses in a pulse train using a sinusoidal reference signal. The duty cycle D varies sinusoidally over time, allowing for smooth control of the output voltage. [16]

In a three-phase Sinusoidal Pulse Width Modulation (S-PWM) system, the duty cycle for each phase is determined by its respective reference voltage.
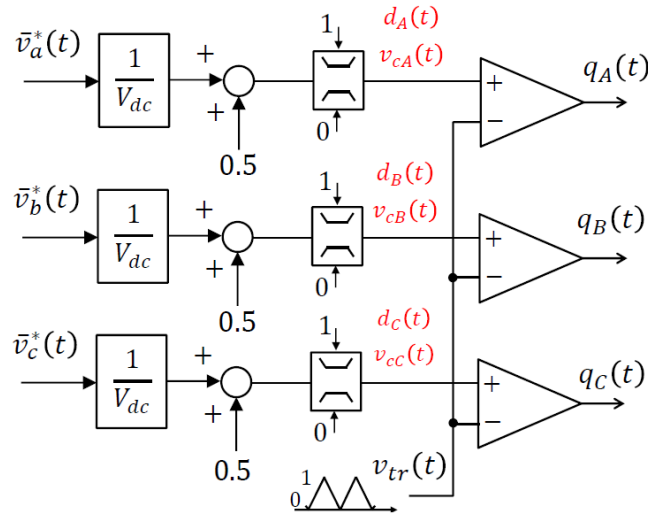
Figure 2.11: Block diagram for Sinusoidal PWM Signal Generation [16]

The duty cycle d for each phase can be calculated as:

$$d_a = \frac{V_{a,\text{ref}}}{V_{dc}} + 0.5 \tag{2.11}$$

$$d_b = \frac{V_{b,\text{ref}}}{V_{dc}} + 0.5 \tag{2.12}$$

$$d_c = \frac{V_{c,\text{ref}}}{V_{dc}} + 0.5 \tag{2.13}$$

where V_{dc} is the DC bus voltage, and $V_{a,\text{ref}}$, $V_{b,\text{ref}}$, and $V_{c,\text{ref}}$ are the reference voltages for phases a, b, and c, respectively. These reference voltages are given by:

$$V_{a,\text{ref}}(t) = V_m \sin(\omega t) \tag{2.14}$$

$$V_{b,\text{ref}}(t) = V_m \sin(\omega t - \frac{2\pi}{3}) \tag{2.15}$$

$$V_{c,\text{ref}}(t) = V_m \sin(\omega t + \frac{2\pi}{3}) \tag{2.16}$$

Here, V_m is the peak value of the reference sinusoidal waveform, and ω is the angular frequency of the reference signal.
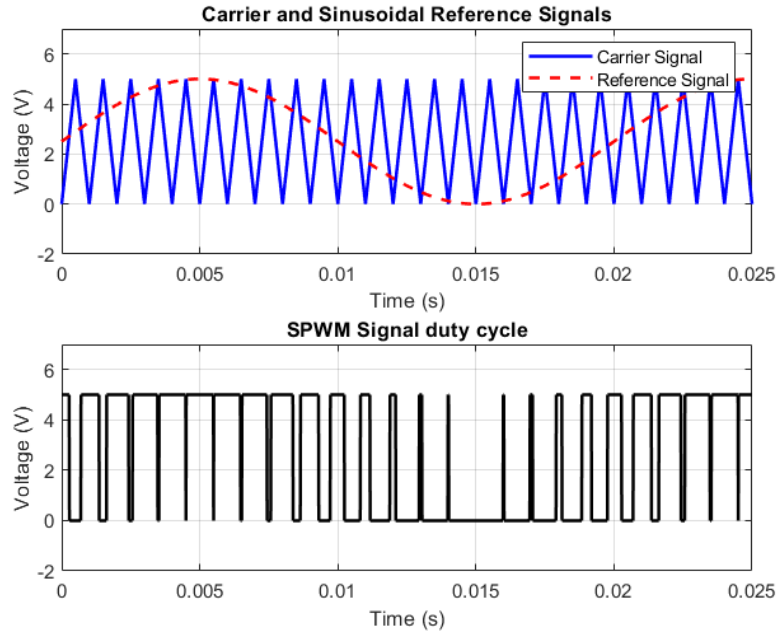
Figure 2.12: Sinusoidal PWM Signal Generation

2.2.6   Regular Sampled S-PWM

In order to extend the linear region of the inverter without resorting to highly complex techniques such as Space Vector Modulation, Regular Sampled Sinusoidal Pulse Width Modulation (RS-SPWM) has been employed. This method focus on the inherent third harmonic rejection of three-phase systems to achieve a 15% increase in output voltage without resorting to overmodulation. Specifically, the third harmonics, being in phase across all three output voltages, cancel out when considering line-to-line voltages, and in a three-wire system, third harmonic currents cannot circulate. Leveraging this phenomenon, a reference signal with a dominant fundamental component, greater than the peak of the carrier signal but with a third harmonic component phased such that the resultant reference signal remains below the carrier's peak, is utilized. Consequently, only the fundamental component influences the load, while the third harmonic is effectively eliminated. [16]
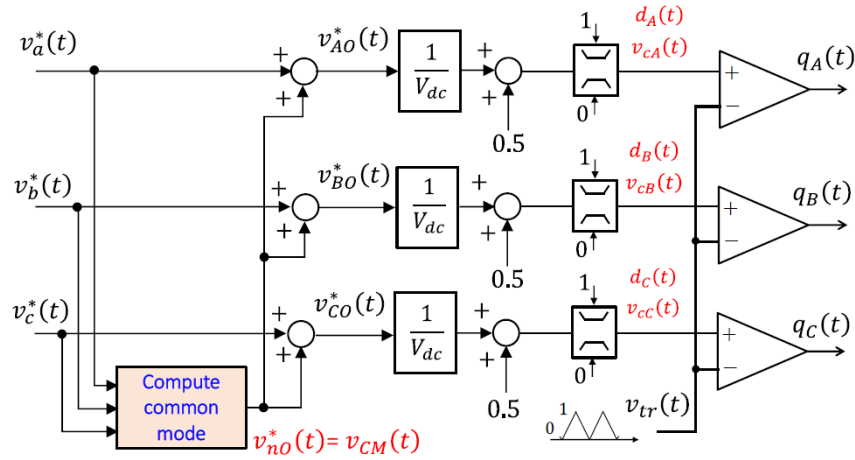
Figure 2.13: RS-SPWM scheme [16]

In Fig. 2.13 it can be seen the scheme of the modulator, which is similar to Fig. 2.12, except for the injection of the v_{cm} in the three-phase reference. The v_{cm}, which is called common mode signal, will be the third harmonic injected, but

need to be calculated. To do so, we need to find the maximum and the minimum voltages:

$$v_{\max} = \max(v_a, v_b, v_c) \tag{2.17}$$

$$v_{\min} = \min(v_a, v_b, v_c) \tag{2.18}$$

and the v_{cm} can be written as:

$$v_{cm} = -\frac{v_{\max} + v_{\min}}{2} \tag{2.19}$$

The entire scheme can be summarised in the scheme 2.14.
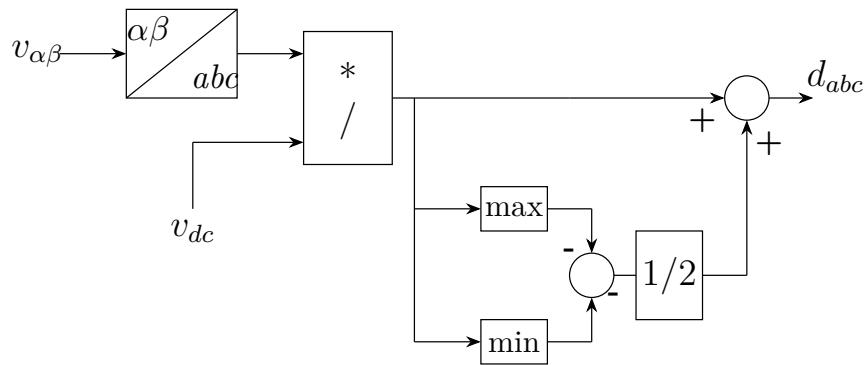
Figure 2.14: RS-SPWM block scheme with common mode calculation

Finally, in 2.15 the reference duty cycles for each phase can be seen.
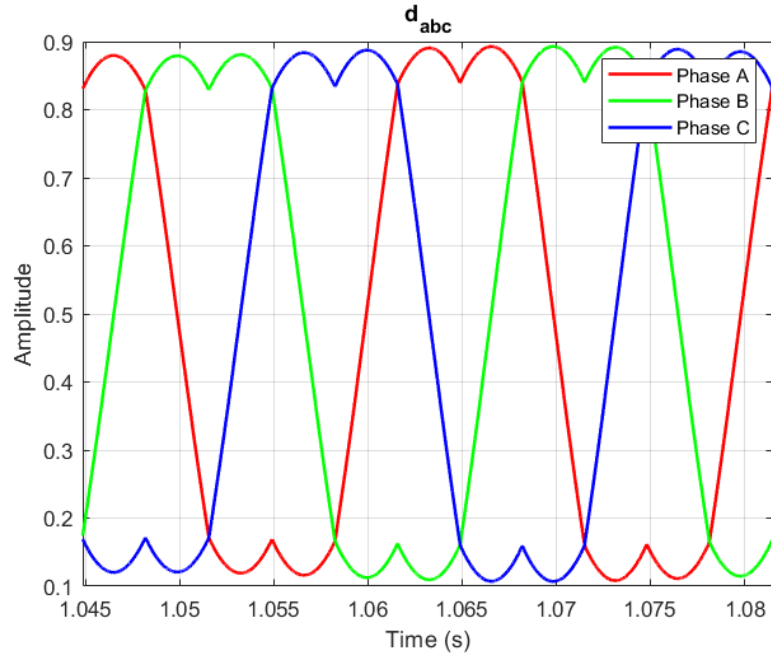
Figure 2.15: Reference d_{abc} with RS-SPWM

2.3   PLECS implementation

In this section, the implementation of the models analyzed in Section 2 using the PLECS software will be illustrated. This includes a detailed description of the simulation setup and a presentation of the obtained results.

For this thesis, it has been decided first to implement the model only on PLECS ambient. After that, the C-script ambient has been implemented and used in order to get the scripts files for the laboratory tests on a real inverter. Thus, it will be presented the final C-script based model.

2.3.1 Grid model and converter on PLECS

Firstly, the entire grid model has been implemented.
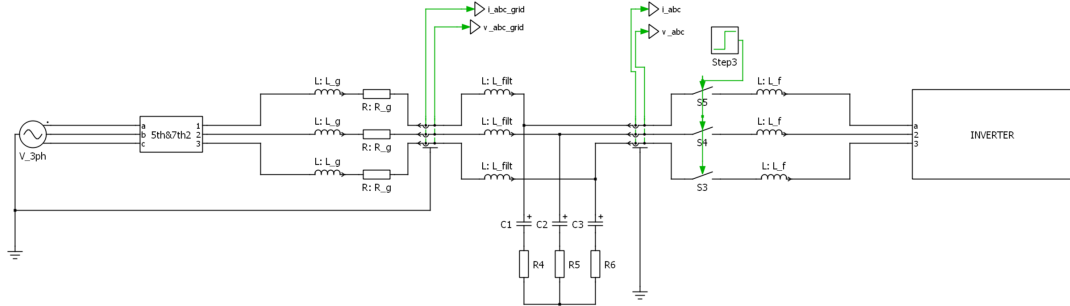
Figure 2.16: PLECS Diagram of Grid model including AFE, LCL filter and Dc-Link

In 2.16 we can see all the components of the grid model:

- Grid model, including the AC Three-Phase ideal generator, R_g and L_g.

- A block which if enabled add some harmonic distortions into the grid, in order to get the simulation more "real".

- LCL filter, including the dumping resistance R_{dump}.

- The mesuraments of the three-phase voltages and currents, taken from the PCC.

- The ideal inverter, which is controlled throught the q_{abc} generated from the control blocks.

After that, we can find the control blocks 2.17, where we can find all the blocks that elaborates the C-Scripts:

- **State Machine** in which the state machine has been implemented, whose purpose is to enable all the blocks in the correct time.

- **Control** in which the scripts of the control are implemented, including PI regulators.

- **Samplings** where the signal get sampled in order to simulate the sampling measurements of a real micro-controller.

- **S-PWM** in which the modulator is implemented.

- **References** in which both i_{dq}^* and PQ^* references can be settled.

- **Impedance Estimation** where the C-scripts for the algorithms of estimation of the grid impedance Z_g are implemented.
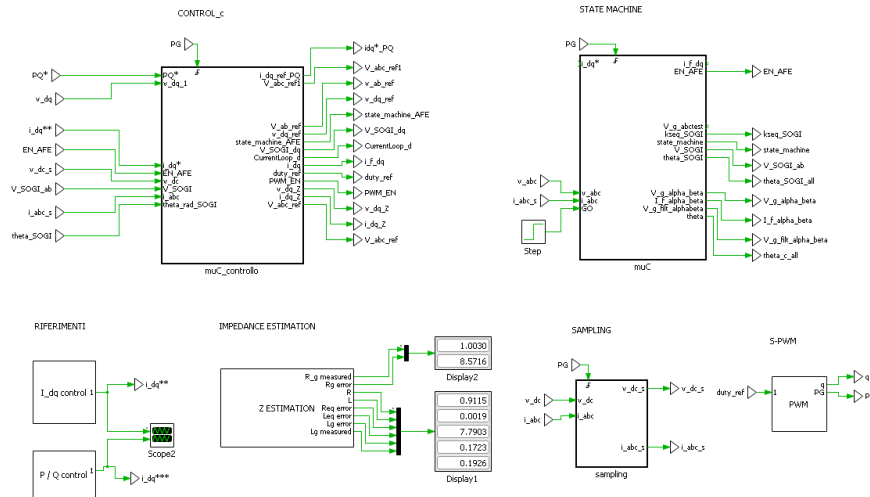
Figure 2.17: Control blocks section

2.3.2 C-Script implementation

As it has been said before, the real implementation of the control on the converter is done on a ISR script written in C. The full code is reported in the Appendix A for reference. In this section the focus is on some technique used in the C-script for the implementation of the converter control.

State machine implementation

First of all, a *State Machine* has been implemented. In this way, the controller is able to manage the connection to the grid and to start the control in the correct way.

- **Sequence detector** In the first stage, the SOGI-filter starts to calculate the filtered voltage and therefor the θ_g which will be used in the control. For a correct implementation of the SOGI-filter, a sequence detector is needed. In fact, it is able to detect if the three-phase system sequence is direct or inverse, which is crucial for a correct estimation for the SOGI-filter.

```
case SEQ_DET:
    if(Vgrid_filt_ab.alpha < 0.0 && valpha_oldSD >= 0.0) {
        if(Vgrid_filt_ab.beta >= 0){
            kseq++;
        } else {
            kseq--;
        } counterSD++;
    }
    if(counterSD >= MAXCOUNT) {
        if ( kseq >0 ) kseqSOGI = -1;
        else kseqSOGI = 1;
        state_machine = SOGI;
    } break;
```

Listing 2.1: Sequence Detector

- **SOGI-filter discretization** The SOGI filter is a second order transfer function, and in order to obtain a good discretization for the implementation of C-script, it is necessary to pass to a state space representation and then discretize it. This work is done in [17] and [18]. Matrices **A** and **B** are then calculated in the *init code*:

```
void init_code(void){
        w_g = 2 * PI * f_grid;
    cost0 = w_g * T_s;
    cost1 = 2 * k_SOGI / w_g;

    A[0] = cos(cost0);
    A[1] = sin(cost0);
    B[0] = cost1 * sin(cost0);
    B[1] = cost1 * ( cos(cost0) - 1 );
}
```

Listing 2.2: A B calculations

To end with, the code for the SOGI-filter discretized has been implemented:

```
void SOGI_filter(double *x1, double *x2, double u){
    double err, output1, output2;   //out - input
    err  = u - *x1;

    output1 =  *x1 * A[0] + *x2 * A[1] + B[0] * err;
    output2 = -*x1 * A[1] + *x2 * A[0] + B[1] * err;

    *x1 = output1;
    *x2 = output2;
}
```

Listing 2.3: SOGI-filter discretized

- **PLL for** θ_g To end with, thanks to the voltages filtered from the SOGI-filter, θ_g can be calculated in this way:

```
1    theta_rad_SOGI = (atan2(V_SOGI.beta, V_SOGI.alpha));
2    if (theta_rad_SOGI > 2*PI) theta_rad_SOGI -= 2*PI;
3    if (theta_rad_SOGI < 0) theta_rad_SOGI += 2*PI;
4 }
```

<div align="center">

Listing 2.4: PLL for θ_g

</div>

In 2.18 is illustrated the final estimated θ_g. When the SOGI-PLL starts to work, it estimate the correct value of θ_g in few moments.

<div align="center">
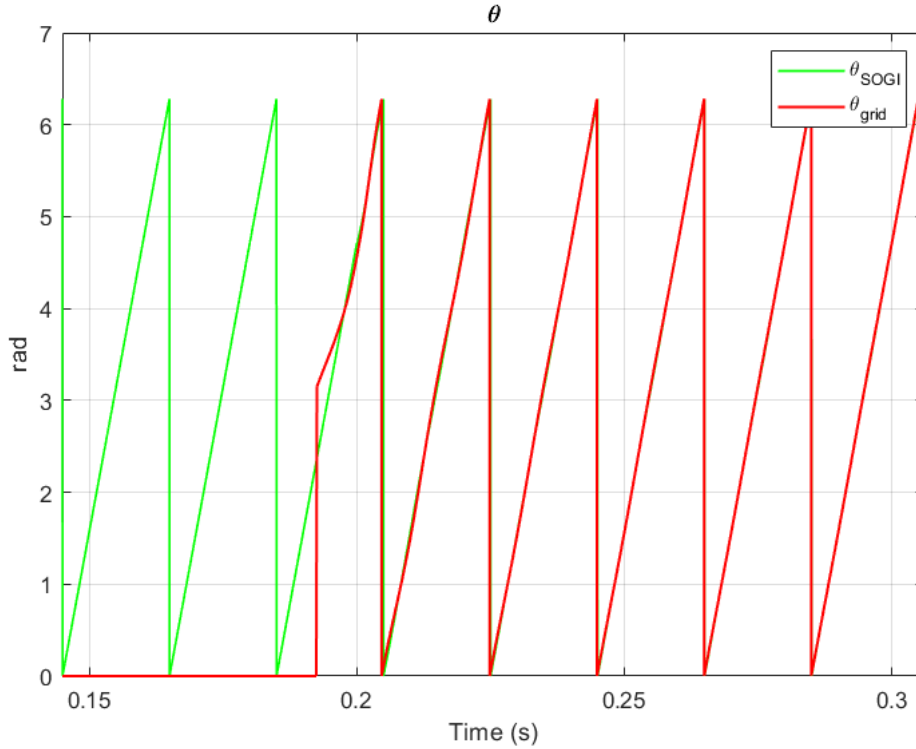
Figure 2.18: θ_g estimated from the SOGI-PLL

</div>

- **AFE state-machine** When the AFE-Enable goes to ON-state, the AFE state machine starts to work, but it also have some stages:

  - *ERROR* In which the code manage the ERROR state (i.e. in case of overcurrent or overvoltage protection)

  - *PRE-CHARGE* In which it is managed the precharge of the capacitors.

  - *GO* where the control starts to work and power starts to flow.

2.4 Parameters settings and simulation results

To end with, in 2.3, all the parameters of the *PLECS* model can be found.

Table 2.3: *PLECS* model parameters

Parameter	Symbol	Value
Grid Voltage	V_{grid}	400 V
Grid frequency	f_{grid}	50 Hz
DC-link	V_{DC}	800 V
Power base	S_b	15 kVA
Voltage base	V_b	400 V
Switching Frequency	f_{sw}	72 kHz
Power base	S_b	15 kVA

In addition, in order to have correct values for the grid impedance, all the values are chosen in per unit. Finally, the impedance is calculated starting from the $theta_{grid}$. In 2.4 all the parameters can be found, and in particular the values chosen for this simulation.

$$Z_b = \frac{V_b^2}{S_b} \tag{2.20}$$

$$R_b = \frac{V_b^2}{S_b} \tag{2.21}$$

$$L_b = \frac{V_b^2}{S_b \times 2\pi 50} \qquad (2.22)$$

$$R_g = Z_g \times \cos(\theta_g) \qquad (2.23)$$

$$L_g = Z_g \times \sin(\theta_g) \qquad (2.24)$$

Table 2.4: Impedance parameters

Parameter	Symbol	Value
Impedance baseline	Z_b	10.7 *ohm*
Resistance baseline	R_b	10.7 *ohm*
Inductance baseline	L_b	0.034 H
θ_{grid}	θ_{grid}	30°
Impedance p.u.	Z_{pu}	0.1 p.u.
Resistance p.u.	R_{pu}	0.86 p.u.
Inductance p.u.	L_{pu}	0.5 p.u.
Impedance	Z_g	1.07 *ohm*
Resistance	R_g	0.92 *ohm*
Inductance	L_g	0.0017 H

For example, it can be seen the results of a simulation in which the request are settled in (2.5), the resulting power absorbed from the grid in 3.5(b) and voltages and currents in 3.5(a).

Table 2.5: Simulation reference parameters

Parameter	Symbol	Value
Active power	P^*	12000 W
Resistance baseline	Q^*	1000 var
θ_{grid}	θ_{grid}	30°

Figure 2.19: In (a) i_{dq} and v_{dq} in the simulation. In (b) Active and Reactive power absorbed from the grid
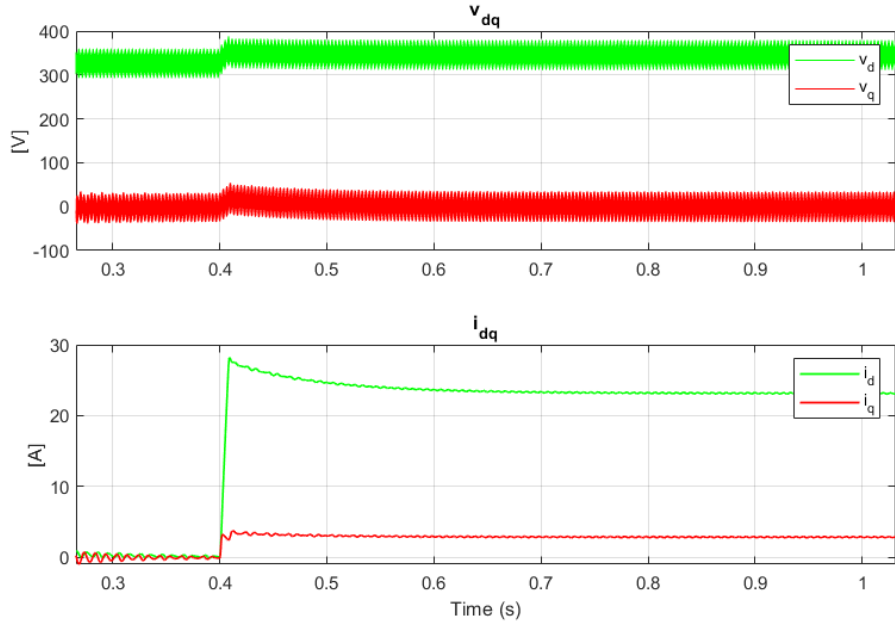
((a))
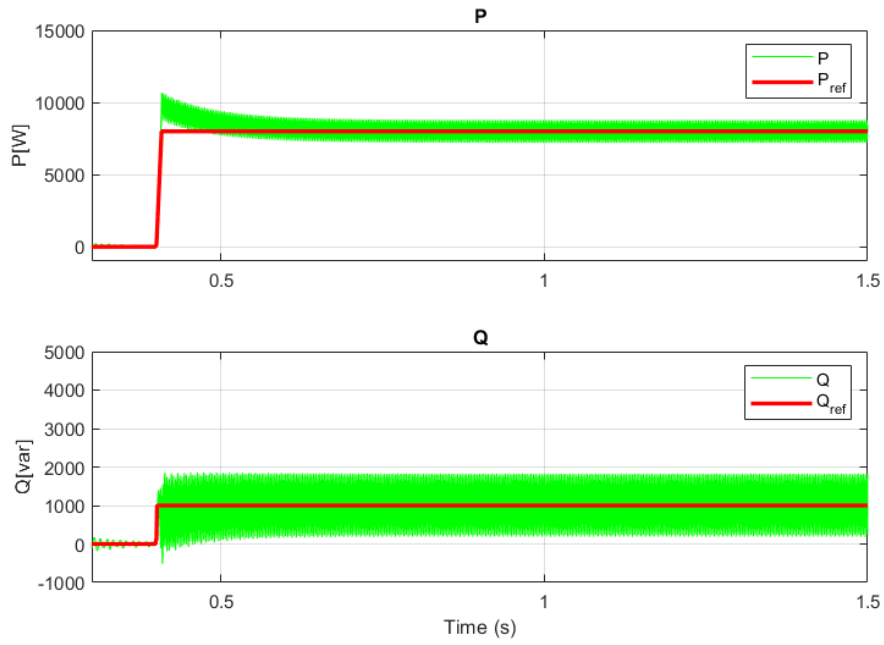
((b))

Chapter 3

Impedance estimation through P/Q variations

In this section, the first technique for the grid impedance estimation Z_g will be analysed and implemented. In this case, the variations on Active and Reactive power references will be used. There are many articles in the literature that uses this type of technique, and some of them will therefore be analysed. [19][20][21][22][23] The method is generally simple and notable for its computational efficiency, which stands out as its primary advantage. In addition, it has been demonstrated that the entire disturb into the grid is not so high, while the error of estimation is low.

3.1   Method description

The method is able to detect grid impedance by varying both active and reactive power generated by a grid-connected generation system. By deliberately altering the references for active and reactive power, the method enables the detection of both the resistive and inductive components of the line impedance. In particular, as follow:

- Introduce P or Q step change

- Take measuraments of voltages and currents in the *dq* domain and in steady state condition (the transient needs to be null).

- Calculate Impedance using algebraic method.

As it can be seen in 3.1, in this method the only modification in the control loop is the addition of ΔP and ΔQ in the references.
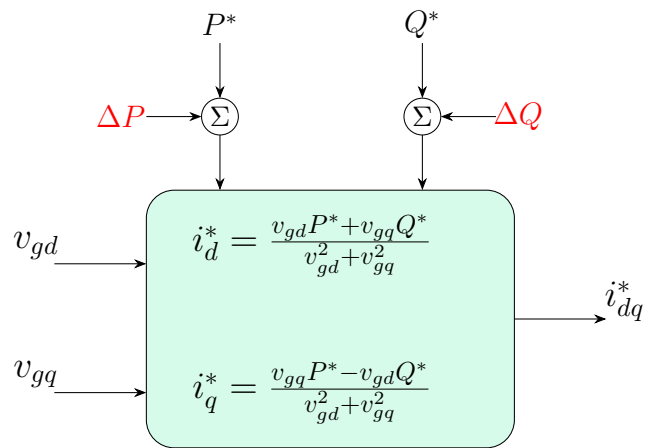
Figure 3.1: Control Scheme with PQ variations
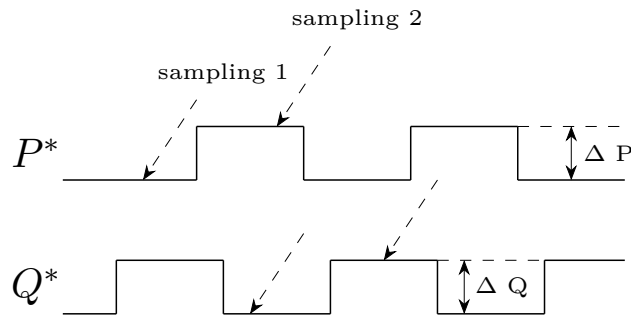
Figure 3.2: Signal references for PQ

46

The signal references are ideally illustrated in 3.2, in which it can be seen the right moment to make the measurements(that needs to be done with currents and voltages). In particular, two samplings needs to be done, in order to get information from two different working point.

The proposed method is based on the detection of dq components of grid voltage and current respectively. The voltage at the point of common coupling in two operating points can be written as:

$$\vec{V}_{pcc1} = \vec{V}_s - Z \cdot \vec{I}_{pcc1} \tag{3.1}$$

$$\vec{V}_{pcc2} = \vec{V}_{s2} - Z \cdot \vec{I}_{pcc2} \tag{3.2}$$

In which 1 and 2 are representing the two different sampling points. After that, the line impedance can be calculated using the variations in both current and voltage at the point of common coupling:

$$Z = \frac{\Delta \vec{V}_{pcc}}{\Delta \vec{I}_{pcc}} \tag{3.3}$$

where:

$$\Delta \vec{V}_{pcc} = \vec{V}_{pcc1} - \vec{V}_{pcc2} \tag{3.4}$$

$$\Delta \vec{I}_{pcc} = \vec{I}_{pcc1} - \vec{I}_{pcc2} \tag{3.5}$$

It is important to notice that the above equations are valid only if the source voltage and grid impedance are not changing between the two sample instants, so $V_s(1) = V_s(2)$

In order to get the grid impedance parameters, it is needed to get current and voltages in the *dq* domain, so that the voltage at the point of common coupling is always referring to a general rotating reference frame provided by θ. Finally, based on the *dq* components of both voltage and current, the resistive and inductive part of the impedance can be calculated in this way:

$$R = \frac{(V_{q1} - V_{q2})(I_{q1} - I_{q2}) + (V_{d1} - V_{d2})(I_{d1} - I_{d2})}{(I_{q1} - I_{q2})^2 + (I_{d1} - I_{d2})^2} \tag{3.6}$$

$$\omega L = \frac{(V_{d1} - V_{d2})(I_{q1} - I_{q2}) - (V_{q1} - V_{q2})(I_{d1} - I_{d2})}{(I_{q1} - I_{q2})^2 + (I_{d1} - I_{d2})^2} \tag{3.7}$$

To estimate the impedance value using this technique, variations in grid voltage and current are required. Given that the changes in input power affect the power delivered to the utility grid, these variations can be used to derive the necessary voltages and currents under two different operating conditions. In general, variations in Active power P^* are not allowed. The proposed method indicates that reactive power variations are essential to induce a phase angle deviation, $\Delta\theta$, at the point of common coupling (PCC). According to interconnection requirements for power generation systems, these systems are permitted to exhibit reactive power variations at the PCC of about 10% of the nominal active power under normal operating conditions. In the follow sections, it will be analysed if the variations of only reactive power Q can be sufficient for having a low estimation error without disturbing the active power delivered into the grid. In addition, some tests will be done, in order to understand the lowest percentage of variations that are sufficient for having an high accuracy in the estimation. By comparing the measurements taken when $P^* = P$ and when $P^* = P + \Delta P$ (similarly for Q), one can obtain ΔV_{pcc} and ΔI_{pcc} necessary for calculating the resistive and inductive components of the impedance.

3.2 PLECS Implementation

In this section it will be illustrated how this technique can be implemented on PLECS and C-script, making some adjustment so that it is suitable for this model and this type of application.

3.2.1 P/Q reference additional variations

Firts of all, some blocks on PLECS are implemented to get the step variations of active and reactive power.

(a)

(b)
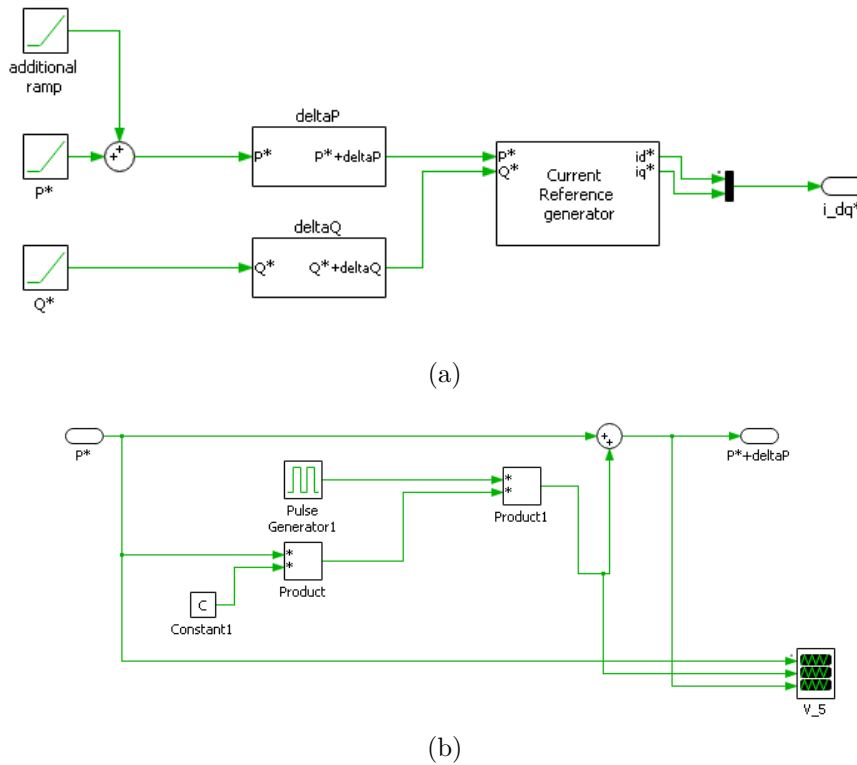
Figure 3.3: (a) the entire block scheme for the reference generation. (b) Inside of the block to make the addition of ΔP

.

In 3.3 the schematic blocks are illustrated. In this implementation, it is possible to choose the percentage of ΔP or ΔQ in respect to the request of Active and

Reactive power. In addition, it is possible to choose the frequency of the impulse and also a time delay to chose the correct moment to make the disturb.

To start with, a first simulation has been implemented, with the parameters settled in 3.1. In particular, it has been decided to not interact with active power so that the load is not disturbed.

Table 3.1: Simulation parameters for P/Q variations

Parameter	Symbol	Value
Active Power	P^*	15 kW
Reactive Power	Q^*	1 kvar
P variation	ΔP	0 W
Q variation	ΔQ	1.5 kvar
Q variation p.u.	ΔQ	0.1 p.u.
Frequency of impulse	f_i	4 Hz

In 3.4, it can be observed how the entire model reacts to this type of variations. It is clear that the reactive power, which is the only parameter with an additional reference, exhibits some step changes. These changes are reflected not only in i_q, but also in v_d and v_q.

Figure 3.4: In (a) i_{dq} and v_{dq} in the simulation with the addtition of a ΔQ on the reference signal. In (b) Active and Reactive power absorbed from the grid
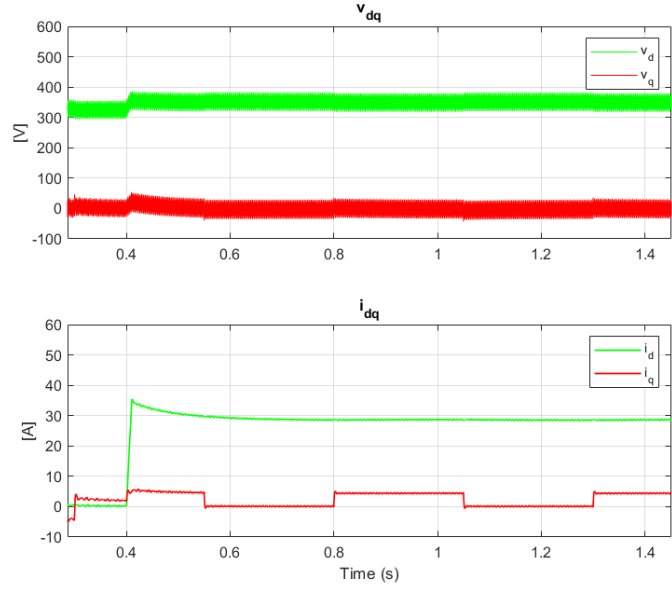
((a))
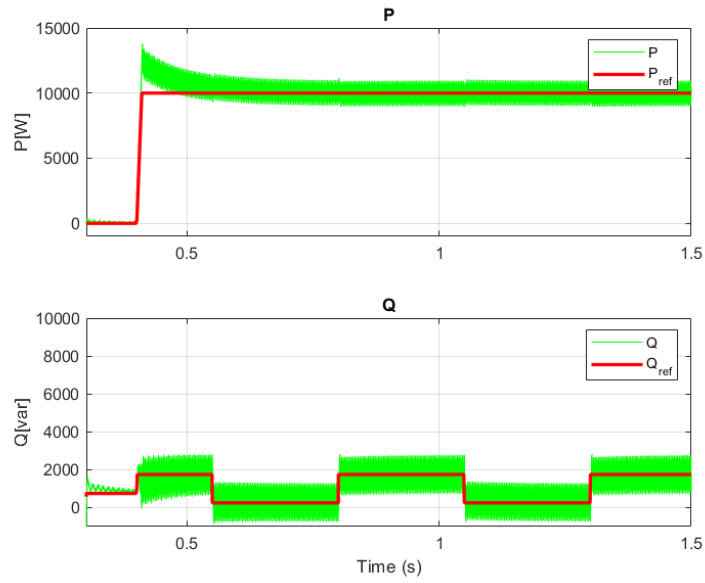
((b))

3.2.2 Grid Impedance estimation algorithm blocks

To estimate the impedance parameters, it is essential to accurately measure the currents and voltages. Firstly, it is crucial to determine the precise moment at which these measurements should be taken. Specifically, the C-script must be synchronized with the impulse generator to ensure correct timing for the measurements. In addition, the values of current and voltage in the *dq* domain needs to be filtered to reduce noise and enhance accuracy.
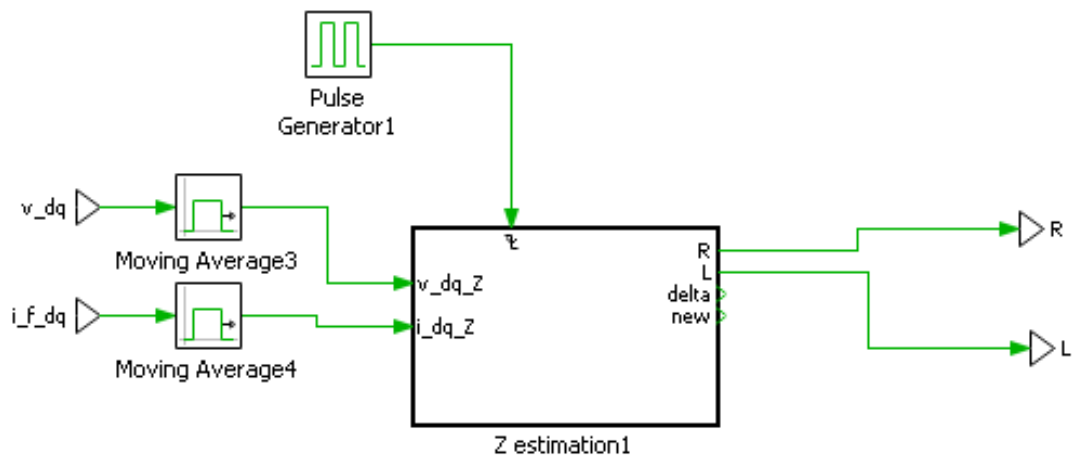
Figure 3.5: Z_g estimation Algorithm block on PLECS

In 3.5 it can be seen that the C-script in the block starts with a frequency generated by an impulse generator, which is synchronized with the impulse of the references. His purpose is to get the measurements in the two working points, to save both of them and finally make the calculation to get the values of R and L

```
1  // INPUT
2  i_dq_Z.d = InputSignal(0,0);
3  i_dq_Z.q  = InputSignal(0,1);
4  v_dq_Z.d = InputSignal(0,2);
5  v_dq_Z.q = InputSignal(0,3);
6  // CODE saves the old value and take the new one
7  i_q.old_dq = i_q.new_dq;
8  i_d.old_dq = i_d.new_dq;
9  v_q.old_dq = v_q.new_dq;
10 v_d.old_dq = v_d.new_dq;
11 v_d.new_dq = v_dq_Z.d;
12 v_q.new_dq = v_dq_Z.q;
13 i_d.new_dq = i_dq_Z.d;
14 i_q.new_dq = i_dq_Z.q;
15 // Calculate the variations
16 v_d.delta_dq = v_d.old_dq - v_d.new_dq;
17 v_q.delta_dq = v_q.old_dq - v_q.new_dq;
18 i_d.delta_dq = i_d.old_dq - i_d.new_dq;
19 i_q.delta_dq = i_q.old_dq - i_q.new_dq;
20
21 // Calculate parameters
22 R = ((v_q.delta_dq) * (i_q.delta_dq)+(v_d.delta_dq)*(i_d.delta_dq
      ))/((i_q.delta_dq)*(i_q.delta_dq) + (i_d.delta_dq)*(i_d.
      delta_dq));
23
24 L = (((v_d.delta_dq) * (i_q.delta_dq)-(v_q.delta_dq)*(i_d.
      delta_dq))/((i_q.delta_dq)*(i_q.delta_dq) + (i_d.delta_dq)*(i_d
      .delta_dq)))/ (2*PI*50);
```

Listing 3.1: Estimation algorithm on C-script for P/Q variations method

3.3 Simulation results

It is now possible to analyze the simulation results and discuss them. Initially, we can configure the simulation to determine if the parameters are correctly detected and to quantify the estimation error. In this simulation, a step change in resistance will be introduced to simulate a real-world scenario, such as islanding detection. This approach allows us to evaluate the algorithm's ability to accurately track the correct parameters under dynamic conditions. In 3.2 the settled parameters.

Table 3.2: Simulation parameters for impedance estimation

Parameter	Symbol	Value
Active power	P^*	10 kW
Reactive Power	Q^*	1 $kvar$
Q variation p.u.	ΔQ	0.05 p.u.
θ_{grid}	θ_{grid}	40°
Impedance	Z_g	1.07 ohm
Resistance	R_g	0.82 ohm
Inductance	L_g	0.0022 H
Step change R	ΔR_g	+50 %

In Fig. 3.6, the final results are presented. It is evident that, after an initial transient period where the model has not yet reached steady-state conditions, it accurately detects the correct values of R_g and L_g. Additionally, Fig. 3.7 illustrates the percentage error, demonstrating good accuracy. During the simulation, a step change in the R_g parameter was introduced at 1.6 s, increasing its base value by 50%. It can be observed that, following the initial transient, the model successfully stabilizes and accurately tracks the correct value in steady-state conditions, thus effectively following the values of the Z_g parameters.

Notably, the error in the inductance L_g is very low, while the resistance R_g maintains an error below 15%. These values are consistent with those calculated in [20]. It is important to note that the step change applied solely to the resistance is

an idealized scenario; in a real grid, variations in impedance Z_g typically occur as rotations of the impedance vector. Hence, the error is higher due to the fact that the grid is not in normal conditions.
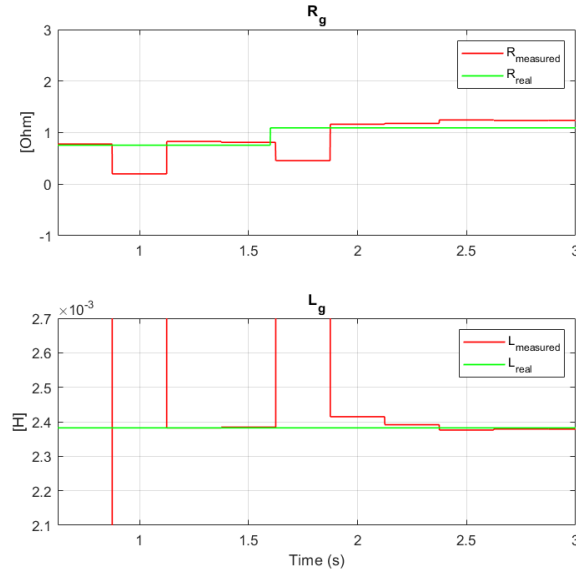
Figure 3.6: Z_g estimations with PQ variations, step change in R_g at 1.6 s
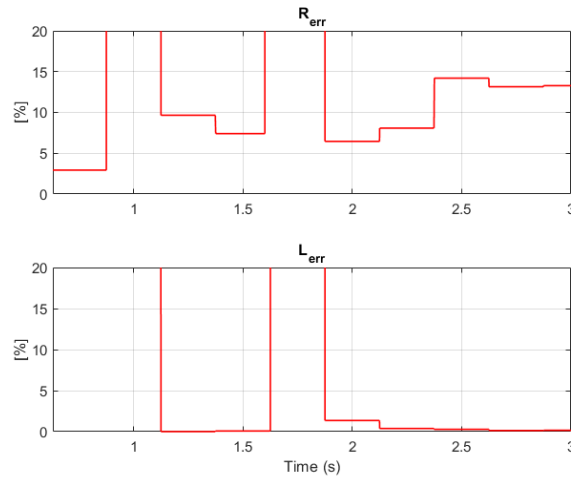
Figure 3.7: Estimation error for R_g and L_g

Chapter 4

Impedance estimation through non-characteristic injections

In this section, the second category of techniques for grid impedance estimation, Z_g, will be analyzed and implemented. This technique involves injecting an excitation at a single non-characteristic frequency, thereby avoiding disturbance of the fundamental frequency. It is crucial to note that this type of analysis assumes a linear impedance. Numerous studies in the literature employ this technique, as referenced in [24, 25, 26, 27]. Although these studies all utilize non-characteristic injections, they may differ in their approaches, using either current or voltage injections at various frequencies (high or low). Consequently, two distinct methods will be examined. The first method, described in [25], employs voltage injection for the disturbance. The second method, detailed in [27], utilizes current injection instead. By comparing these two approaches, we can gain insights into different methodologies for estimating grid impedance. In 4.1, the block diagram illustrates

the injection process for both options. It can be observed how the injection occurs, providing a visual representation of the methodology employed for grid impedance estimation.
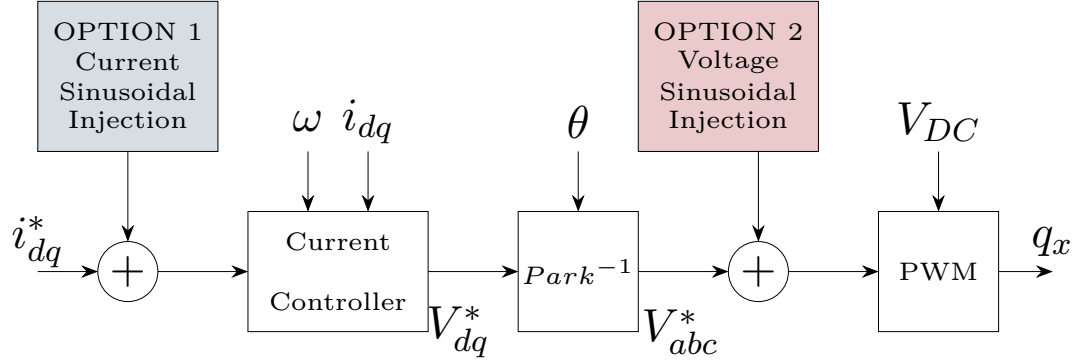
Figure 4.1: Block scheme for injection methods

4.1 Voltage injection method description

The first method is described in [25]. There are two type of approach:

- **Single harmonic injection(SH)** in which, a single voltage injection is implemented.

- **Double harmonic injection(DH)** in which, two voltage injection at different frequencies are implemented.

Single harmonic injection(SH)

In this method, the grid-connected inverter injects harmonic current by incorporating a harmonic voltage into the inverter's voltage reference, as depicted in Fig. 4.1. The harmonic injection occurs at the zero voltage crossing point. Consequently, the impact on the active power produced by the grid-connected inverter is minimized. The expected result is illustrated in Fig. 4.2, where a voltage

harmonic injection has been implemented. Specifically, a 600 Hz sinusoidal signal with a 50 V amplitude has been injected.
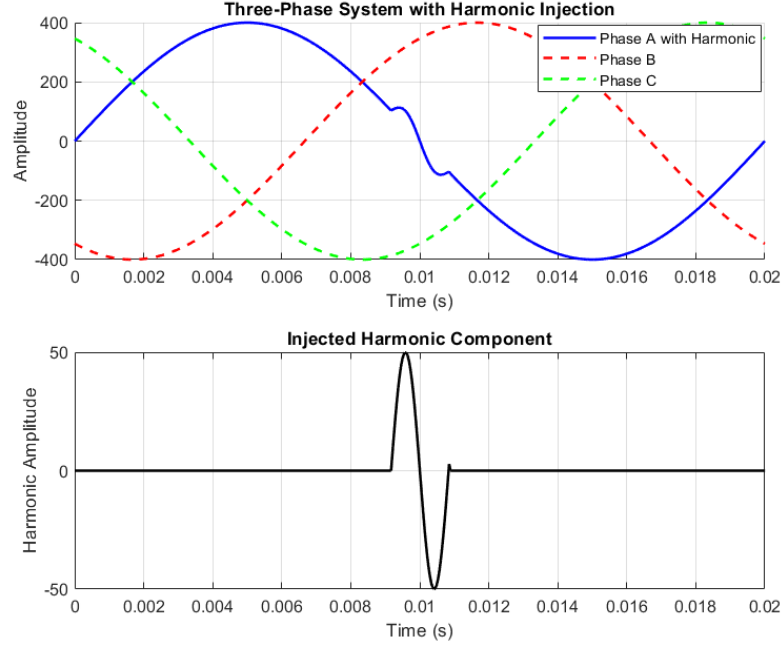
Figure 4.2: Voltage Harmonic injection

The single harmonic is injected into the grid, and the response of the injection is measured using voltage and currents values. The signals are further analyzed using Discrete Fourier Transformation (DFT), enabling the derivation of amplitude and phase information. In particular a moving DFT has been implemented:

$$\hat{X}_h = \sum_{n=0}^{N-1} x_n \left(\cos\left(\frac{2\pi h n}{N}\right) - i \cdot \sin\left(\frac{2\pi h n}{N}\right) \right) \tag{4.1}$$

$$\hat{X}_h = x_{hr} + i \cdot x_{hi} \tag{4.2}$$

In which:

- **N** is the number of samples;

58

- **h** is the harmonic that has been chosen;

- x_n is the input signal, in this case current or voltage signal;

- $\hat{X}_h$ is the corresponding complex Fourier vector of the k harmonic;

- x_{hr} and x_{hi} are the real and immaginary part of the Fourier vector.

In order to get the estimated values of Z_g parameters, the calculations are done in this way. Firstly, as it can be seen in 4.3, the fundamental frequency components are subtracted in order to reduce the noise. The signals are then analysed by the DFT, which is able to extract only the component for a chosen frequency.
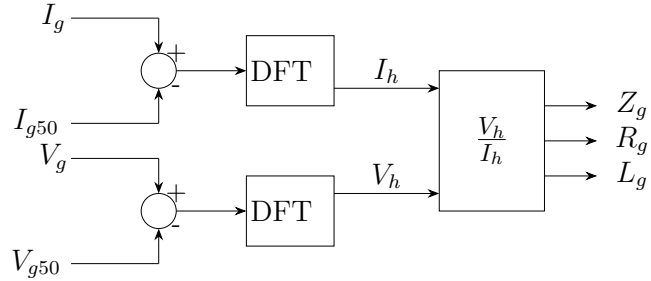
Figure 4.3: Block diagram for the SH method

Finally, thanks to this equations we can calculate the parameters.

$$\hat{Z}_h = R_g + i \cdot w_h L_g; \tag{4.3}$$

$$\hat{Z}_h = \frac{\hat{V}_h}{\hat{I}_h} \tag{4.4}$$

$$R_g = real(\hat{Z}_h) \tag{4.5}$$

$$L_g = \frac{imag(\hat{Z}_h)}{w_h} \tag{4.6}$$

59

Double harmonic injection(DH)

This method differs from the previous one by utilizing two distinct harmonic injections. The grid-connected inverter injects harmonic currents by incorporating harmonic voltages into the inverter's voltage reference, as illustrated in Fig. 4.1. The harmonic injections occur at the zero voltage crossing point. The expected result is depicted in Fig. 4.4, where 400 Hz and 600 Hz sinusoidal signals with a 50 V amplitude are injected.
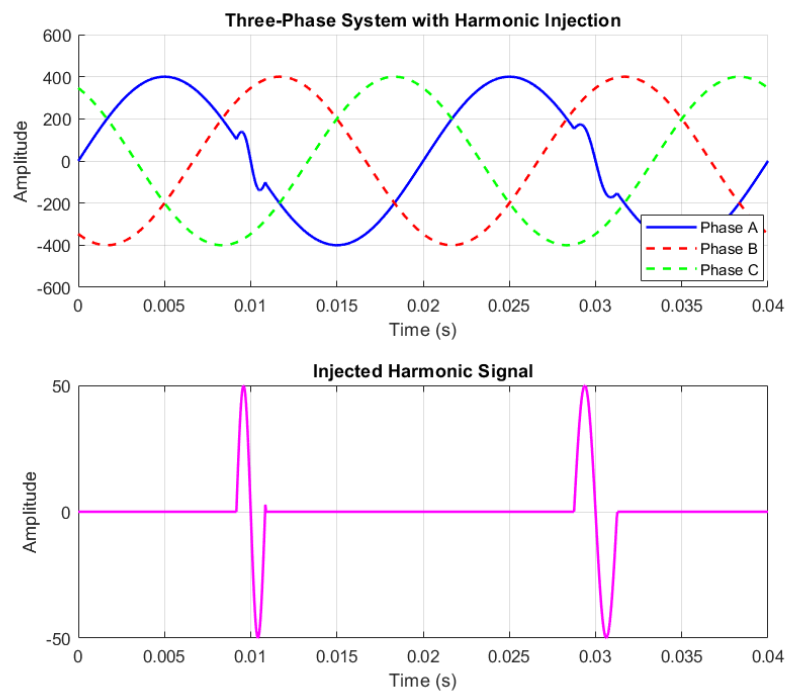
Figure 4.4: Voltage harmonic injection with two different frequencies

This method does not employ the Discrete Fourier Transform (DFT). Instead, it assesses the current response to these perturbations. Specifically, it calculates the mean absolute value of the current response at the frequency of the injected harmonic. 4.5
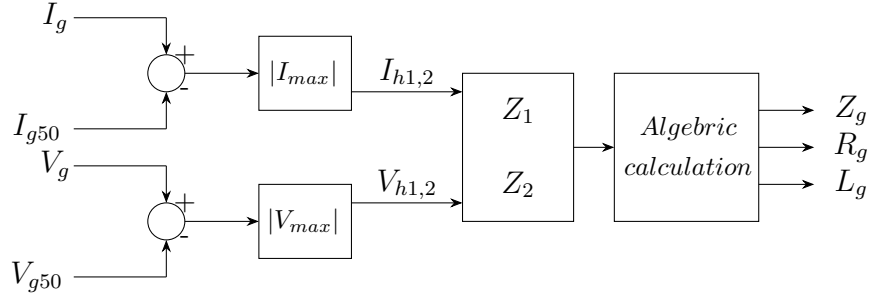
Figure 4.5: Block diagram for the DH method

By evaluating the grid impedance at two distinct points (i.e., using two injected harmonics at different frequencies), the grid parameters can be determined by solving the following set of equations:

In order to calculate the grid resistance R_g and inductance L_g from two impedance measurements Z_1 and Z_2 at angular frequencies ω_1 and ω_2, respectively, we start by expressing the squared magnitudes of the impedances:

$$|Z_1|^2 = R_g^2 + (\omega_1 L_g)^2 \tag{4.7}$$

$$|Z_2|^2 = R_g^2 + (\omega_2 L_g)^2 \tag{4.8}$$

Subtracting these two equations to eliminate R_g^2, we obtain:

$$|Z_1|^2 - |Z_2|^2 = (\omega_1 L_g)^2 - (\omega_2 L_g)^2 \tag{4.9}$$

Factorizing the right-hand side:

$$|Z_1|^2 - |Z_2|^2 = L_g^2(\omega_1^2 - \omega_2^2) \tag{4.10}$$

Solving for L_g, we get:

$$L_g = \sqrt{\frac{|Z_1|^2 - |Z_2|^2}{\omega_1^2 - \omega_2^2}} \tag{4.11}$$

Next, we can substitute L_g back into one of the original equations to solve for R_g:

$$R_g = \sqrt{|Z_1|^2 - (\omega_1 L_g)^2} \tag{4.12}$$

Thus, the grid resistance R_g and inductance L_g are given by:

$$L_g = \sqrt{\frac{|Z_1|^2 - |Z_2|^2}{\omega_1^2 - \omega_2^2}} \tag{4.13}$$

$$R_g = \sqrt{\frac{\omega_1^2|Z_2|^2 - \omega_2^2|Z_1|^2}{\omega_1^2 - \omega_2^2}} \tag{4.14}$$

4.2 Current injection method description

The second technique differs from the first one (Section 4.1), as it implements the injection through current variations instead of voltage variations. As depicted in Fig. 4.1, the current references are modified by adding a non-characteristic current. This method is implemented in [24], where a 75 Hz current is specifically utilized.

Regarding the theoretical description of this technique, it is similar to the single harmonic injection described in Section 4.1. The primary difference is that the injection is applied over a time interval that may vary depending on the specific situation. The resulting current can be seen in 4.6.
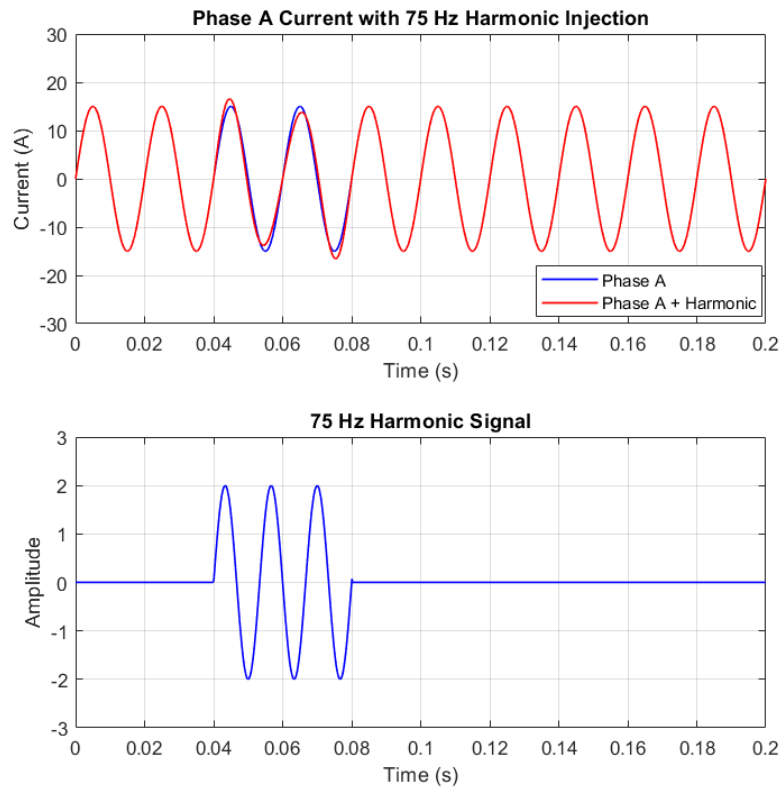
Figure 4.6: Current harmonic injection 75 Hz

After the addition of the current, the signals are analyzed using the same Discrete Fourier Transform (DFT), which will be briefly reviewed here for convenience.

$$\hat{X}_h = \sum_{n=0}^{N-1} x_n \left(\cos\left(\frac{2\pi hn}{N}\right) - i \cdot \sin\left(\frac{2\pi hn}{N}\right) \right) \tag{4.15}$$

$$\hat{X}_h = x_{hr} + i \cdot x_{hi} \tag{4.16}$$

Finally, thanks to this equations we can calculate the parameters.

$$\hat{Z}_h = R_g + i \cdot w_h L_g; \tag{4.17}$$

$$\hat{Z}_h = \frac{\hat{V}_h}{\hat{I}_h} \tag{4.18}$$

$$R_g = real(\hat{Z}_h) \tag{4.19}$$

$$L_g = \frac{imag(\hat{Z}_h)}{w_h} \tag{4.20}$$

It is important to notice that the only substantial difference from the first method is the frequency of the harmonic, that in this case is closer to the fundamental frequency. The DFT yields voltage and current values at a specific injected harmonic frequency. However, standards typically mandate impedance values at the fundamental frequency. Consequently, a conversion from the injected frequency to the fundamental frequency is necessary. Obtaining precise values for Z and ω can be challenging. Therefore, it is often more practical to select a frequency closer to the fundamental frequency, such as 75 Hz.

4.3 PLECS implementation

In this section it will be illustrated how this techniques can be implemented on PLECS and C-script, making some adjustment so that they are suitable for this model and this type of application. All these methods have been implemented in PLECS. However, the first method (SH) utilizing a 600 Hz injection does not perform adequately due to the previously mentioned issue. Consequently, only the Double Harmonic Injection method and the current injection method, will be described in the implementation section.

4.3.1 Double harmonic voltage injection

To implement this method in PLECS, a way for injecting voltage harmonics through the C-script was first developed. Specifically, it is necessary to add a sinusoidal signal with a precise frequency to the reference voltages. Additionally, this signal must be perfectly synchronized with the fundamental voltages, as the injection needs to occur precisely at the zero crossing. To achieve this, the PLL and the known value of θ_g can be used.

In the control C-script, an algorithm has been implemented to determine the precise moment for the injection. This algorithm generates a sinusoidal signal in the dq domain and subsequently adds it to the voltage references V_{abc}^*. Additionally, the algorithm includes functionality to switch the injection frequency at each time interval.

```
1  if(INJ_EN == ON){
2
3      if( inj == 1 && theta_rad_SOGI >= 1  && theta_rad_SOGI <=
   1.5 ) {
4          f_inj = f_inj1;
5        delta_theta = ((f_grid)/f_inj)*PI;
6      }
```

```
7
8          if ( inj == 2 && theta_rad_SOGI >= 1  && theta_rad_SOGI <=
     1.5 ) {
9              f_inj = f_inj2;
10             delta_theta = ((f_grid)/f_inj)*PI;
11         }
12
13         if(theta_rad_SOGI >= (1.69 - delta_theta)  &&
     theta_rad_SOGI <= (1.69 + delta_theta)){
14
15             inj_case= ON;
16             thref = thref + 2*PI*f_inj*T_s;
17
18             v_dq_inj.d = v_in;
19             v_dq_inj.q = 0;
20
21             v_ab_inj = dq_alpha_beta(v_dq_inj.d, v_dq_inj.q, thref)
     ;
22             V_ab_ref.alpha = V_ab_ref.alpha+v_ab_inj.alpha;
23             V_abc_ref = alpha_beta_abc(V_ab_ref.alpha, V_ab_ref.
     beta);
24         } else {
25          thref = 0;
26          inj_case = OFF;
27         }
28
29         if (cambio % 2 == 0) {
30           inj = 1;
31         } else {
32           inj = 2;
33         }
34
35         if(thref == 0 && f == 0) {
```

66

```
36          cambio++;
37          f = 1;
38       } else if(thref != 0) f = 0;
39 }
```

Listing 4.1: Harmonic injection algorithm on C-script

The resulting injection signals can be seen in Fig. 4.7. In particular, the first injection at 600 hz and the second one at 400 Hz. In this case, it has been chosen to add the alpha signal. Finally, we can see the resulting reference variation and the current response. 4.8
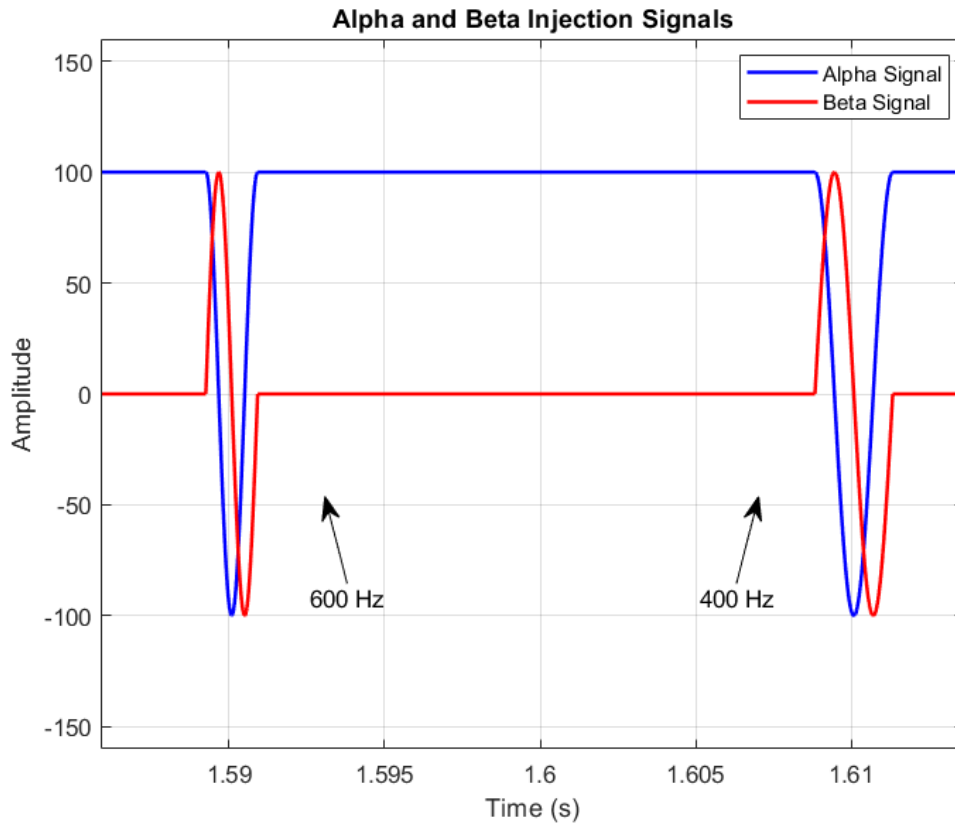
Figure 4.7: Voltage harmonic injection with two different frequencies, PLECS implementation
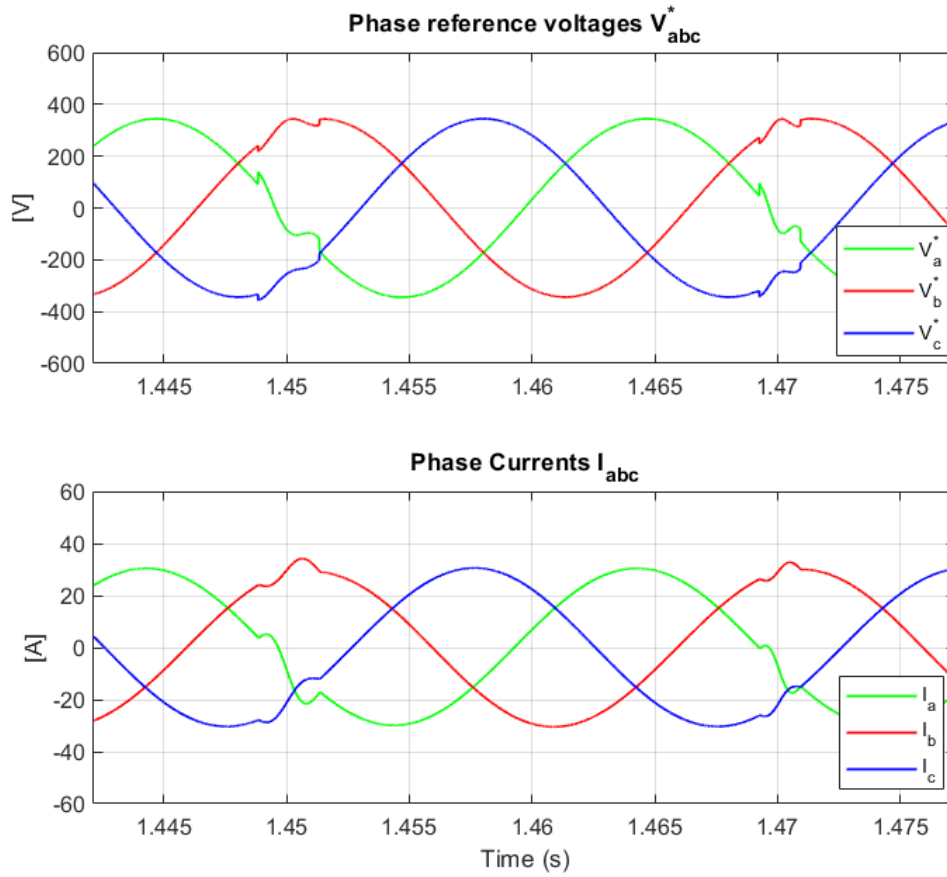
Figure 4.8: V_{abc}^* voltage reference, I_{abc} current response signals with double harmonic injection, PLECS implementation

To conclude, a C-script containing an algorithm capable of estimating the grid parameters will be presented. This algorithm calculates the absolute maximum values for the current and voltage responses, based on the measurements taken at the Point of Common Coupling (PCC). As it can be seen in 4.5, the measurements are firstly filtered, so that only the 400 Hz and 600 Hz can be analysed in the algorithm. After that, the script is able to save the maximum values of current and voltages for each injection and calculate the impedance.

```
1
2  f_inj_2 = 400;
3  f_inj_1 = 600;
4  w_h1 = 2*PI*f_inj_1;
5  w_h2 = 2*PI*f_inj_2;
6  w_h1q = w_h1*w_h1;
7  w_h2q = w_h2*w_h2;
8  w_hd = w_h1q-w_h2q;
9
10  switch(state_machine_INJ){
11     case ERROR:
12          n = 0;
13          V_h1 = 0;
14          I_h1 = 0;
15          V_h2 = 0;
16          I_h2 = 0;
17          max_valueI1 = 0;
18          max_valueV1 = 0;
19          max_valueI2 = 0;
20          max_valueV2 = 0;
21
22          if( INJ_EN == ON) state_machine_INJ = GO;
23
24     break;
25
26     case GO:
27
28          if(inj_case == ON && inj_v == 1) {
29
30                if (V > max_valueV1) {
31                   max_valueV1 = V;
32                }
```

```
33              if (I > max_valueI1) {
34                  max_valueI1 = I;
35                }

36
37       v_h1 = max_valueV1;
38              i_h1 = max_valueI1;

39
40      } else if(inj_case == OFF && inj_v == 1){

41
42          if(v_h1 != 0 && i_h1 != 0) Z_h1 = (v_h1/i_h1);
43          max_valueI1 = 0;
44          max_valueV1 = 0;
45      }

46

47

48      if( inj_case == ON && inj_v == 2) {

49
50              if (V > max_valueV2) {
51                  max_valueV2 = V;
52                }

53
54              if (I > max_valueI2) {
55                  max_valueI2 = I;
56                }

57
58              v_h2 = max_valueV2;
59              i_h2 = max_valueI2;

60
61      } else if(inj_case == OFF && inj_v == 2){

62
63          if(v_h2 != 0 && i_h2 != 0) Z_h2 = (v_h2/i_h2);
64          max_valueI2 = 0;
65          max_valueV2 = 0;
```

```
66        }
67
68
69        L = sqrt(fabs(((Z_h1*Z_h1)-(Z_h2*Z_h2))/w_hd));
70
71        R = sqrt(fabs(((((w_h1q*(Z_h2*Z_h2))-(w_h2q*(Z_h1*Z_h1)))))/
   w_hd));
72
73     if( INJ_EN == OFF ) state_machine_INJ = ERROR;
74   break;
75 }
```

Listing 4.2: Estimation algorithm on C-script for DH method

4.3.2 Current injection at 75 Hz

Some modifications need to be applied to the existing model to achieve current injections instead of voltage injections. Additionally, it has been decided to inject the current harmonics continuously, as done in [24]. In a real-world application, it might be beneficial to inject the current at specific time intervals to maintain a low Total Harmonic Distortion (THD) value. The frequency of these intervals can be adjusted based on the required level of grid observation.

To do so, the current references in the C-script are modified, with an additional signal. This algorithm generates a sinusoidal signal in the *dq* domain and subsequently adds it to the current references I^*_{abc}. Additionally, the algorithm includes a way to select the frequency of injections, the amplitude and also a way to inject the current harmonics in time intervals, in order to get a lower THD value.

```c
if(INJ_EN == ON){

    if(thref < 0) thref += 2*PI;
    else if (thref > 2*PI) thref -= 2*PI;

    thref = thref + 2*PI*25*T_s;
    i_dq_inj.d = i_in;
    i_dq_inj.q = 0;

    i_ab_inj = dq_alpha_beta(i_dq_inj.d, i_dq_inj.q, thref);

        I_dq_ref.d +=i_ab_inj.alpha;
        I_dq_ref.q +=i_ab_inj.beta;
}
```

Listing 4.3: Current injection generation on C-script

The resulting injection signals and the resulting current response can be seen in Fig. 4.9.

72
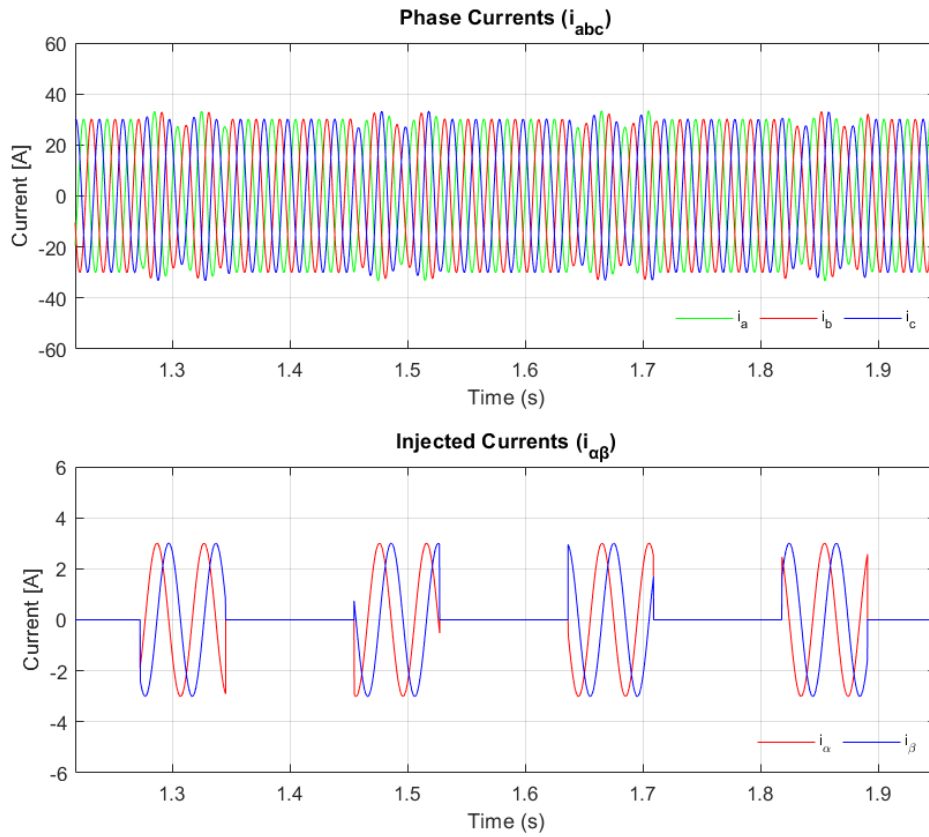
Figure 4.9: I_{abc}^* current reference, $I_{\alpha\beta}$ injection signals at 75Hz, PLECS implementation

After the implementation of the current injections, an algorithm to estimate the impedance parameters has been constructed. As discussed in Section 4.2, this technique utilizes the Discrete Fourier Transform (DFT). Once the measurements are taken and the fundamental frequency component is subtracted, the resulting current and voltage values are analyzed using the DFT, which is implemented in a C-script.

73

```
1
2  N = 960;
3  ang = (2 * PI * (1))/N;
4  f_inj = 75;
5  w=2*PI*f_inj;
6
7  switch(state_machine_INJ){
8
9      case ERROR:
10
11          n = 0;
12          DFT_V.re = 0;
13          DFT_V.im = 0;
14          DFT_I.re = 0;
15          DFT_I.im = 0;
16
17        if( INJ_EN == ON) state_machine_INJ = GO;
18
19      break;
20
21      case GO:
22          n++;
23          if (n < N) {
24          DFT_V.re = DFT_V.re + V * cos( (ang * n));
25          DFT_V.im = DFT_V.im - V * sin( (ang * n));
26
27          DFT_I.re = DFT_I.re + I * cos( (ang * n));
28          DFT_I.im = DFT_I.im - I * sin( (ang * n));
29           }
30
31          if (n == (N-1)) {
32              Z = divisioncpx(DFT_V, DFT_I);
```

```
33              R = Z.re;
34              L = Z.im/(w);
35              n = 0;
36
37              dft_V.re = DFT_V.re;
38              dft_V.im = DFT_V.im;
39              dft_I.re = DFT_I.re;
40              dft_I.im = DFT_I.im;
41              DFT_V.re = 0;
42          DFT_V.im = 0;
43          DFT_I.re = 0;
44          DFT_I.im = 0;
45              }
46
47          if( INJ_EN == OFF ) state_machine_INJ = ERROR;
48      break;
49 }
```

Listing 4.4: DFT estimation algorithm on C-script for current injection method

4.4   Simulation results

It is now possible to analyze the simulation results and discuss them. Initially, we can configure the simulation to determine if the parameters are correctly detected and to quantify the estimation error. As in the last simulation, a step change in resistance will be introduced to simulate a real-world scenario, such as islanding detection. This approach allows us to evaluate the algorithm's ability to accurately track the correct parameters under dynamic conditions. In 4.1 the settled parameters for both the injection methods.

Table 4.1: Simulation parameters for non-characteristic injections

Parameter	Symbol	Value
Active power	P^*	10 kW
Reactive Power	Q^*	1 $kvar$
θ_{grid}	θ_{grid}	45°
Impedance	Z_g	1.06 ohm
Resistance	R_g	0.75 ohm
Inductance	L_g	0.0024 H
Step change R	ΔR_g	+20 %

Double Harmonic voltage injection method simulation results

Firstly, in 4.2, the setting parameters for the injection.

Table 4.2: Simulation parameters for DH method

Parameter	Symbol	Value
Harmonic injection amplitude	V_{inj}	50 V
Frequency 1	f_1	600 Hz
Frequency 2	f_2	400 Hz

Figure 4.10 presents the final results, showing that the model accurately identifies the correct values of R_g and L_g after an initial transient period. During this period, the model has not yet reached steady-state conditions. Additionally, Figure 4.11

displays the percentage error, indicating a high level of accuracy. As with previous methods, a step change in the R_g parameter was introduced at 3 seconds, increasing its base value by 20%. It can be seen that, once past the initial transient phase, the model stabilizes and effectively tracks the correct values of the Z_g parameters in steady-state conditions.
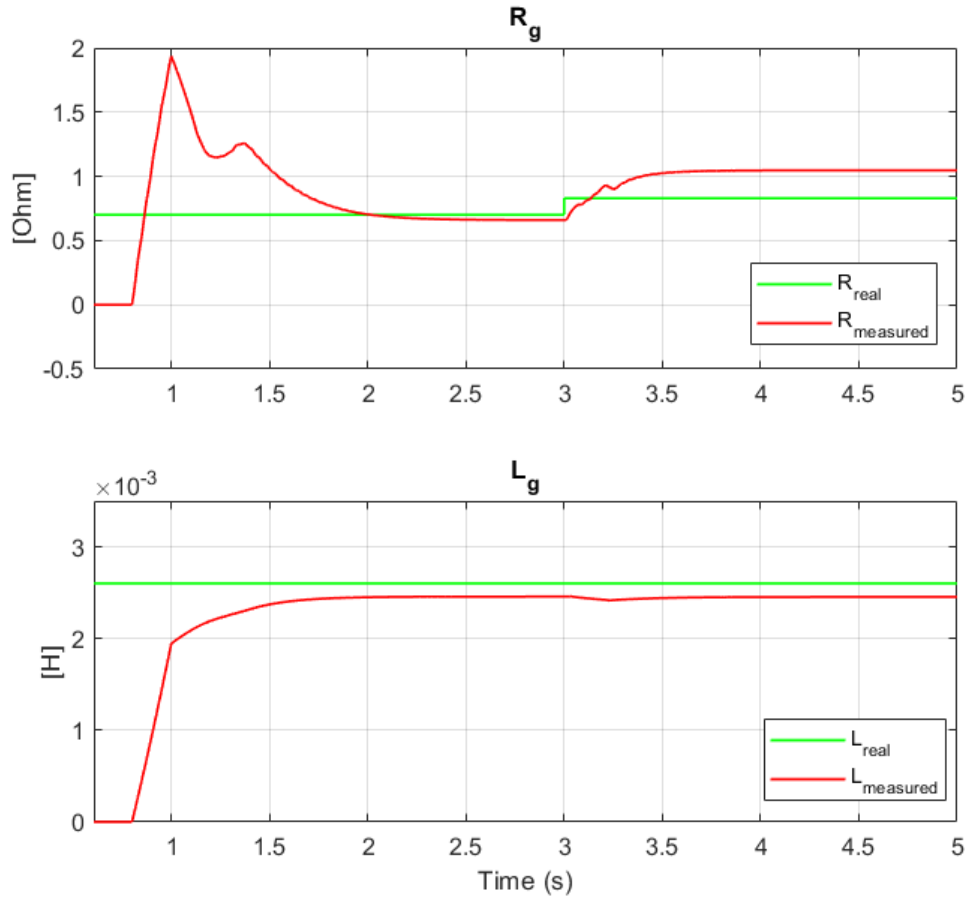
Figure 4.10: Z_g estimations with DH method, step change in R_g at 3 s

The inductance L_g shows a very low error, while the resistance R_g maintains an error below 10% in normal conditions and 30% with the step change. It is worth noting that the step change applied solely to the resistance is an idealized scenario. In a real grid, impedance Z_g variations typically occur as rotations of the

impedance vector, which explains the higher error observed under these non-ideal conditions. Moreover, this method requires a longer time to achieve an accurate estimation compared to other techniques.
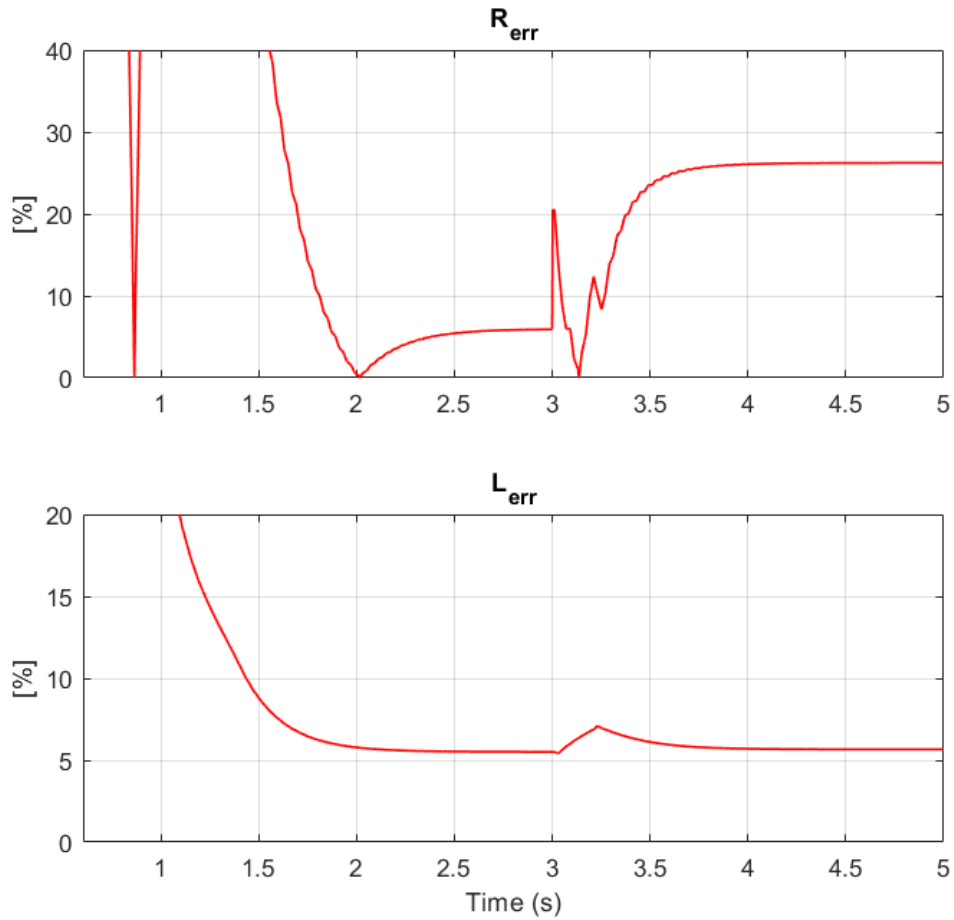
Figure 4.11: Estimation error for R_g and L_g, DH method

75 Hz current injection method simulation results

Firstly, in 4.3, the setting parameters for the injection.

Table 4.3: Simulation parameters for 75 Hz method

Parameter	Symbol	Value
Harmonic injection amplitude	I_{inj}	$3\ A$
Frequency	f_1	$75\ Hz$

In Fig. 4.12, the final results are displayed. It is evident that after an initial transient period, where the model has not yet achieved steady-state conditions, it accurately detects the correct values of R_g and L_g. Moreover, Fig. 3.7 shows the percentage error, indicating good accuracy. During the simulation, a step change was applied to the R_g parameter at 1.6 seconds, increasing its base value by 20%. It can be observed that, following the initial transient, the model successfully stabilizes and accurately tracks the correct values in steady-state conditions, effectively following the Z_g parameter variations.

It is particularly noteworthy that the error in the inductance L_g is very low, while the resistance R_g maintains an error below 10% in steady-state. These values align with those calculated in [24]. It should be noted that the step change applied solely to the resistance represents an idealized scenario; in a real grid, variations in impedance Z_g typically occur as rotations of the impedance vector. Consequently, the higher error observed is attributable to the grid operating in non-standard conditions.
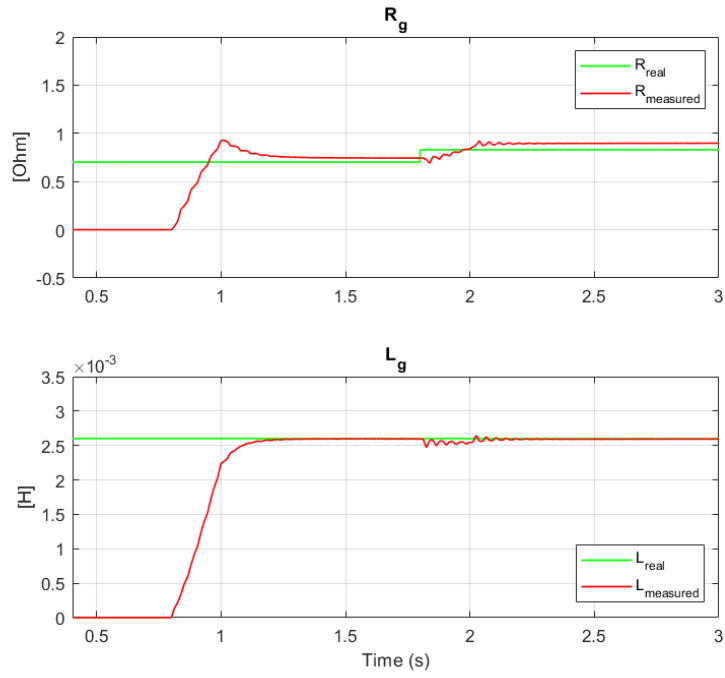
Figure 4.12: Z_g est. with 75 Hz current injection, step change in R_g at 1.8 s
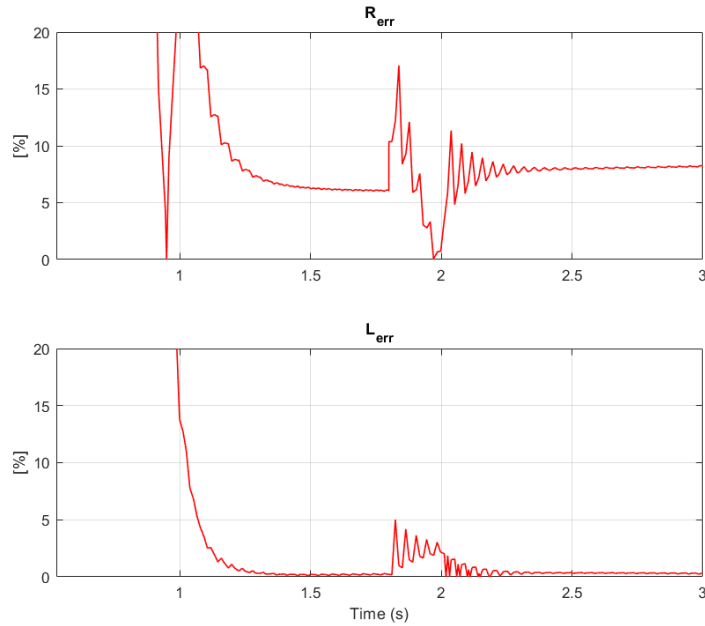
Figure 4.13: Estimation error for R_g and L_g, 75 Hz current injection method

Chapter 5

Performance comparison of estimation algorithms

In this section, a performance evaluation of all the methods will be implemented, in order to compare the different solutions. Firstly it can be implemented a study in which we evaluate the performance of each method changing the percentage of disturbances into the grid (injected harmonics or reactive power variations), in order to find a balance between the THD value and the estimation error. Secondly, each method will be simulated for different grid conditions.

5.1 Simulation for different percentage of disturbances

5.1.1 P/Q variation method

For the first method, the percentage change in reactive power (ΔQ) relative to the base power (S_b) can be adjusted to evaluate the performance under different scenarios. Given a base power $S_b = 15\text{kW}$, we can simulate for ΔQ values of

0.1 pu, 0.05 pu, and 0.01 pu. These values represent variations of 10%, 5%, and 1% of S_b applied to the references, respectively. By varying ΔQ, we can analyze how different magnitudes of reactive power changes impact the accuracy of grid parameter estimation methods.

Table 5.1: ΔQ in pu and its corresponding value for Base Power $S_b = 15\text{kW}$

ΔQ (pu)	ΔQ (kVar)
0.01	0.15
0.05	0.75
0.1	1.5

Table 5.2: Comparison of Errors in R and L

ΔQ (pu)	Error in R (%)	Error in L (%)
0.01	8.62	0.13
0.05	7.79	0.19
0.1	7.70	0.19

In Table 5.2, the estimation errors corresponding to different percentages of changes in the reactive power reference are presented. It is evident that the inductance L_g is accurately estimated across all levels of injected power. On the other hand, the resistance R_g is also estimated with low error. As shown in Table **??**, the estimation error tends to be higher when the variation in reactive power is lower. However, the difference in the error percentage across various levels of reactive power variation is not significant. Therefore, it is not necessary to introduce high variations in reactive power, as the benefit does not outweigh the increased disturbances.

5.1.2   75 Hz current injection method

For the second method, the amplitude of the injected current can be adjusted. Specifically, Table 5.3 shows the selected values of injected current in per unit (PU), based on $I_{\text{base}} = 21.65$ A. This allows for the comparison of different percentages of injected current and their respective performances in the estimation of impedance.

Current (PU)	Current (A)
0.05	1
0.09	2
0.14	3

Table 5.3: Current values in per unit based on $I_{\text{base}} = 21.65$ A

Injected Current	Error in R (%)	Error in L (%)	$THD_V(\%)$	$THD_I(\%)$
1 A	2.75	6.92	4.6	3
2 A	6.50	1.61	4.7	5.6
3 A	8.10	0.59	4.8	8.4

Table 5.4: Comparison of Errors in R and L with different injected currents

Finally, in Table **??**, the resulting estimation errors for different amplitudes of injected current are shown. It can be seen that the parameter L_g is well estimated in all cases, but it reaches the lowest error with a higher current amplitude. On the other hand, the parameter R_g exhibits a lower error with the lowest current amplitude. Additionally, the Total Harmonic Distortion (THD) values for both voltage and current, extracted from the simulations, show that higher injected currents result in higher THD. Therefore, it is preferable to use 1 A or 2 A depending on the situation to balance the estimation errors for R_g and L_g while maintaining the lowest possible THD.

5.1.3   DH Voltage injection method

For the third method, the amplitude of the injected voltage can be modified. Specifically, Table 5.5 shows the selected values of injected voltage in per unit (PU), based on $V_{\text{base}} = 400$ V. This allows for the comparison of different percentages of injected voltages and their respective performances in the estimation of impedance.

Injected Voltage (PU)	Injected Voltage (V)
0.050	20
0.125	50
0.175	70

Table 5.5: Injected voltage values in per unit based on $V_{\text{base}} = 400$ V

Injected Current	Error in R (%)	Error in L (%)	$THD_V(\%)$	$THD_I(\%)$
20 V	16.3	6.8	5.2	3.4
50 V	5.4	6.02	6.6	8.3
70 V	2.4	5.9	8	11

Table 5.6: Comparison of Errors in R and L with different injected voltages

Finally, in Table **??**, the resulting estimation errors for different amplitudes of injected voltages are shown. It can be seen that the parameter L_g is estimated in all cases with a low error. It reaches the lowest error with a higher voltage amplitude. On the other hand, the parameter R_g is not well estimated with a low amplitude injection. It exhibits a lower error with the highest voltage amplitude. Additionally, the Total Harmonic Distortion (THD) values for both voltage and current, extracted from the simulations, show that higher injected voltages result in higher THD, also reaching not acceptable values. Therefore, it is preferable to use 50 V voltage injections to balance the estimation errors for R_g and L_g while maintaining the lowest possible THD.

5.2 Simulation for different Grid Conditions

The simulation of varying grid conditions necessitates the precise adjustment of key electrical parameters, specifically the phase angle θ_g and the X/R ratio. The phase angle θ_g dictates the phase difference between the grid voltage and current, which influences the reactive power flow within the system. By systematically varying θ_g, we can replicate a spectrum of grid conditions ranging from predominantly inductive to predominantly resistive behaviors. Various θ_g reflects on the X/R ratio, which denotes the ratio of reactance (X) to resistance (R). In particular, the short-circuit ratio (SCR) of the simulated grid is kept constant at 10.

$$SCR = \frac{Z_b}{Z_g} = 10 \tag{5.1}$$

In Fig. 5.1, these aspects are graphically represented, showing the X/R ratio as a function of θ_g and highlighting the different areas of interest.
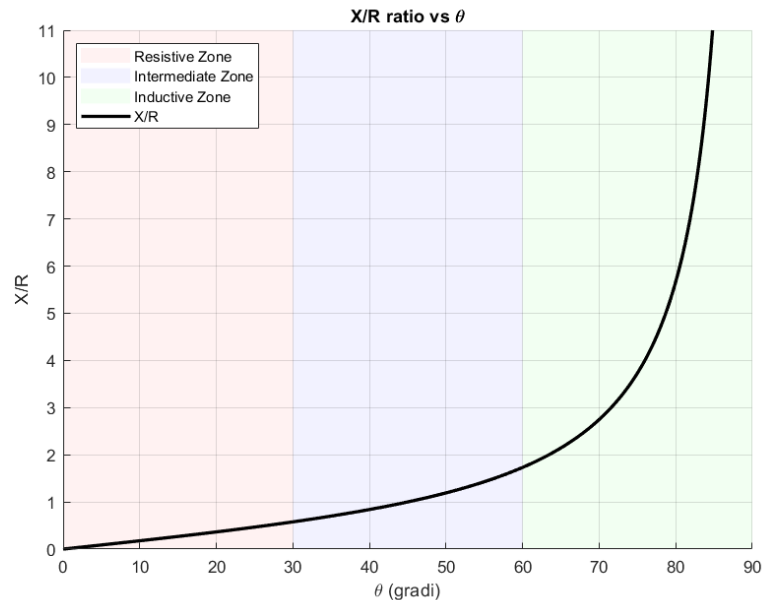
Figure 5.1: X/R ratio in function of θ_g

85

In our simulations, conducted within the PLECS environment, the grid model comprises a three-phase electrical network with adjustable parameters such as grid impedance (Zg), grid voltage (V_g), and grid frequency (f_g). To emulate different grid conditions, θ_g is varied to introduce different phase shifts, hence the X/R ratio is adjusted by independently modifying the inductive and resistive components of the network impedance. This variation allows for a comprehensive analysis of grid behavior under a wide range of conditions. By examining the resultant impacts on the grid's performance, we can evaluate the effectiveness of all grid parameter estimation methods, ensuring their robustness and reliability across diverse and dynamic grid scenarios.
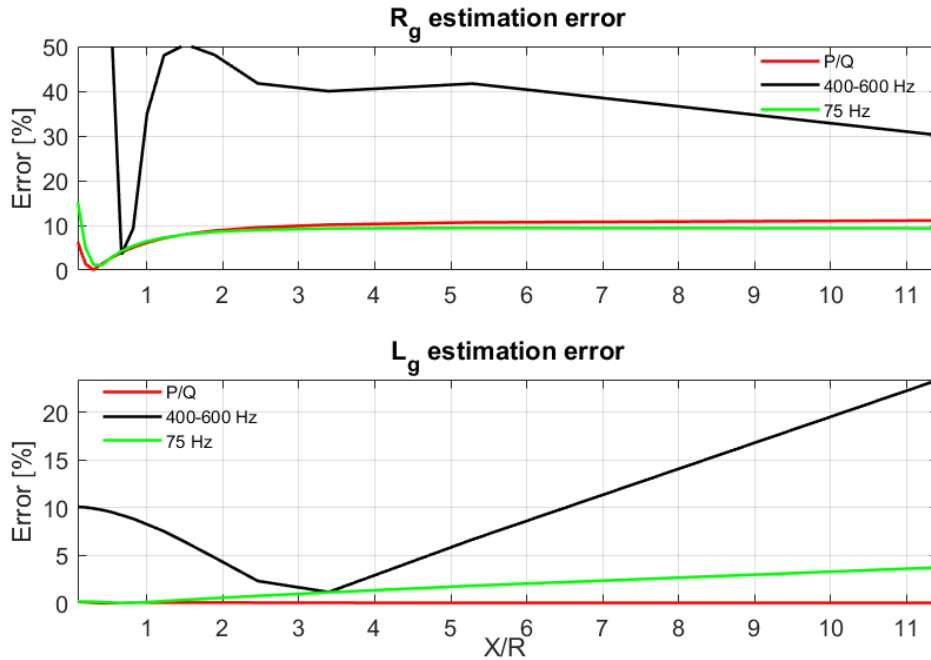
Figure 5.2: Comparison of the three methods varying X/R

In Fig. 5.2 the final estimation results. It illustrates a comparative analysis of all the methods applied in a simulation study where the grid conditions vary in terms of the X/R ratio and θ_g. The methods involving P/Q variations and 75

Hz current injections demonstrate superior robustness compared to the Double Injection method. These methods consistently yield low estimation errors across a wide range of grid conditions. In particular, when the grid operates within its normal range, both methods achieve a nearly zero error in estimation. However, even under highly resistive or inductive grid conditions, the estimation error remains below 10%. In contrast, the Double Injection method exhibits significant limitations, particularly in accurately estimating R_g under extreme grid conditions characterized by high inductance or high resistance. The estimation accuracy of R_g deteriorates substantially when the grid exhibits either a predominantly inductive or resistive behavior. Consequently, while the Double Injection method may perform adequately in less extreme scenarios, it is not recommended for grids with highly variable or extreme inductive and resistive properties. The robustness of the P/Q variations and 75 Hz current injection methods makes them more suitable for diverse and challenging grid environments, ensuring better performance and stability in real-world applications.

Chapter 6

Conclusions

The primary aim of this study was to research, analyse and evaluate methods for real-time estimation of grid impedance using ultra-fast charging stations. This work was driven by an initial literature review that highlighted the limitations of passive techniques for real-time estimation. Passive methods, while simpler, were found to be less effective especially for real-time estimation of grid parameters.

In the course of this research, active techniques were chosen due to their superior ability to provide accurate and timely impedance estimations. These techniques involve deliberate perturbation of the grid and measurement of the response, which is critical for the reliable operation of ultra-fast charging stations.

Furthermore, the selection process for the estimation techniques was influenced by the need to minimize computational overhead. Micro-controllers in Active Front End (AFE) converters have limited computational resources, making it essential to use methods that are not computationally intensive. Therefore, techniques that are very precise but computationally complex were deliberately excluded in favor of sufficiently accurate but simpler methods that are easier to process.

To validate the proposed methods, an inverter model connected to the grid was implemented in the PLECS simulation environment. This allowed for the

generation of results that are closer to real-world scenarios. Additionally, all the methods were implemented in the PLECS environment and as C-scripts, enabling their deployment in laboratory applications.

Both the P/Q variations and 75 Hz current injections methods demonstrated superior robustness and low estimation errors across various grid conditions, ensuring errors below 10%. In contrast, the Double Injection method showed significant limitations, particularly under highly resistive or inductive grid conditions.

This research contributes to the field of power systems by analysing reliable techniques for real-time impedance estimation, useful for the stability and efficiency of ultra-fast charging stations. The ability to accurately estimate grid impedance in real time can enhance the performance of charging infrastructure, supporting the widespread adoption of electric vehicles.

Despite the success of the proposed methods, there were challenges in estimating impedance under extreme grid conditions, indicating areas for improvement. Future work could focus on minimizing the network disturbances introduced by the effective P/Q variation and current injection methods, further enhancing their applicability and reliability.

Appendix A

C-scripts code

Output Function Code for State Machine

```
1
2  // INPUT signals
3
4  Vgrid_abc.a = InputSignal(0,0);
5  Vgrid_abc.b = InputSignal(0,1);
6  Vgrid_abc.c = InputSignal(0,2);
7
8  I_abc.a = InputSignal(0,3);
9  I_abc.b = InputSignal(0,4);
10 I_abc.c = InputSignal(0,5);
11
12 go_state = InputSignal(0,6);
13
14 // CODE
15
16 //Transformation matrices
17  Vgrid_alphabeta = abc_alpha_beta( Vgrid_ph_abc.a, Vgrid_ph_abc.b,
       Vgrid_ph_abc.c);
```

```
18  Vgrid_abc_test = alpha_beta_abc(Vgrid_ph_alphabeta.alpha,
        Vgrid_ph_alphabeta.beta);

19

20  //Low pass filter
21  Vgrid_filt_ab.alpha = filter(Vgrid_ph_alphabeta.alpha, valpha_old
        , kfilt);
22  Vgrid_filt_ab.beta = filter(Vgrid_ph_alphabeta.beta, vbeta_old,
        kfilt);

23

24  I_alphabeta =  abc_alpha_beta(I_f_abc.a, I_f_abc.b, I_f_abc.c);

25

26  valpha_old = Vgrid_filt_alphabeta.alpha;
27  vbeta_old = Vgrid_filt_alphabeta.beta;
28  u = Vgrid_ph_alphabeta.alpha;
29  in = I_f_alphabeta.alpha;

30

31

32  //STATE MACHINE

33

34  switch(state_machine){

35

36      case INIT:

37

38      valpha_oldSD = Vgrid_filt_alphabeta.alpha;

39

40      if( go_state == TRUE ) state_machine = SEQ_DET;

41

42

43      break;

44

45

46      case SEQ_DET:  // Sequence detector state

47
```

```
48    if(Vgrid_filt_ab.alpha < 0.0 && valpha_oldSD >= 0.0) {
49        if(Vgrid_filt_alphabeta.beta >= 0){
50        kseq++;
51        } else {
52        kseq--;
53        }
54
55    counterSD++;
56
57    }
58
59    if(counterSD >= MAXCOUNT) {
60
61        if ( kseq >0 ) kseqSOGI = -1;
62        else kseqSOGI = 1;
63
64        state_machine = SOGI;
65    }
66
67    valpha_oldSD = Vgrid_filt_alphabeta.alpha;
68
69
70    break;
71
72    case SOGI: //Second Order Generalized Integrator
73
74
75    SOGI_filter(&V_SOGI_temp.alpha, &V_SOGI_temp.beta, u);
76
77    V_SOGI.alpha = V_SOGI_temp.alpha;
78    V_SOGI.beta = V_SOGI_temp.beta*kseqSOGI;
79
80    SOGI_filter(&i_SOGI_temp.alpha, &i_SOGI_temp.beta, in);
```

```
82      I_SOGI.alpha = i_SOGI_temp.alpha;
83      I_SOGI.beta = i_SOGI_temp.beta*kseqSOGI;
84
85      EN_AFE = 1;
86
87      break;
88
89  }
90
91      // Theta calculation using filtered voltages
92
93      theta_rad = (atan2(Vgrid_ph_alphabeta.beta, Vgrid_ph_alphabeta
        .alpha));
94      if (theta_rad > 2*PI) theta_rad -= 2*PI;
95      if (theta_rad < 0) theta_rad += 2*PI;
96
97      theta_rad_SOGI = (atan2(V_SOGI.beta, V_SOGI.alpha));
98      if (theta_rad_SOGI > 2*PI) theta_rad_SOGI -= 2*PI;
99      if (theta_rad_SOGI < 0) theta_rad_SOGI += 2*PI;
100
101 // OUTPUT
102
103 OutputSignal(0, 0) = Vgrid_ph_ab.alpha;
104 OutputSignal(0, 1) = Vgrid_ph_ab.beta;
105 OutputSignal(0, 2) = I_f_alphabeta.alpha;
106 OutputSignal(0, 3) = I_f_alphabeta.beta;
107 OutputSignal(0, 4) = Vgrid_filt_ab.alpha;
108 OutputSignal(0, 5) = Vgrid_filt_ab.beta;
109 OutputSignal(0, 6) = theta_rad;
110 OutputSignal(0, 7) = cos(theta_rad);
111 OutputSignal(0, 8) = sin(theta_rad);
112 OutputSignal(0, 9) = Vgrid_ph_abc_test.a;
```

```
113 OutputSignal(0, 10) = Vgrid_ph_abc_test.b;
114 OutputSignal(0, 11) = Vgrid_ph_abc_test.c;
115 OutputSignal(0, 12) = kseqSOGI;
116 OutputSignal(0, 13) = state_machine;
117 OutputSignal(0, 14) = V_SOGI.alpha;
118 OutputSignal(0, 15) = V_SOGI.beta;
119 OutputSignal(0, 16) = theta_rad_SOGI;
120 OutputSignal(0, 17) = cos(theta_rad_SOGI);
121 OutputSignal(0, 18) = sin(theta_rad_SOGI);
122 OutputSignal(0, 21) = EN_AFE;
123 OutputSignal(0, 22) = I_SOGI.alpha;
124 OutputSignal(0, 23) = I_SOGI.beta;
125 }
```

Listing A.1: C code for State Machine

Output Function Code for control loop

```
1  // INPUT SIGNALS
2
3  V_SOGI.alpha = InputSignal(0,0);
4  V_SOGI.beta  = InputSignal(0,1);
5  I_f_abc.a = InputSignal(0,2);
6  I_f_abc.b = InputSignal(0,3);
7  I_f_abc.c = InputSignal(0,4);
8  I_dq_ref.d = InputSignal(0,5);
9  I_dq_ref.q = InputSignal(0,6);
10 theta_rad_SOGI = InputSignal(0,7);
11 EN_AFE = InputSignal(0,8);
12 v_dc = InputSignal(0,9);
13 P_ref = InputSignal(0,10);
14 Q_ref = InputSignal(0,11);
15 v_dq_1.d = InputSignal(0,12);
16 v_dq_1.q = InputSignal(0,13);
```

```
17  v_inj.a = InputSignal(0,14);
18  v_inj.b = InputSignal(0,15);
19  v_inj.c = InputSignal(0,16);
20  INJ_EN = InputSignal(0,17);
21
22  // CODE
23
24   I_f_alphabeta =  abc_alpha_beta(I_f_abc.a, I_f_abc.b, I_f_abc.c);
25   I_f_dq = alpha_beta_dq(I_f_alphabeta.alpha, I_f_alphabeta.beta,
        theta_rad_SOGI);
26   V_SOGI_dq = alpha_beta_dq(V_SOGI.alpha, V_SOGI.beta,
        theta_rad_SOGI);
27
28   // Generation of current refeerences from Akagi theory
29   I_ref_PQ.d = ((P_ref*V_SOGI_dq.d)-(Q_ref*V_SOGI_dq.q))/(V_SOGI_dq
        .q*V_SOGI_dq.q+V_SOGI_dq.d*V_SOGI_dq.d);
30   I_ref_PQ.q =((P_ref*V_SOGI_dq.q)+(Q_ref*V_SOGI_dq.d))/(V_SOGI_dq.
        q*V_SOGI_dq.q+V_SOGI_dq.d*V_SOGI_dq.d);
31
32
33  // STATE MACHINE AFE
34
35  switch(state_machine_AFE){
36
37      case ERROR:
38
39      PWM_EN = OFF;
40      EN_DFT = OFF;
41      n = 0;
42      f = 0;
43
44      if( EN_AFE == TRUE )  {
45
```

```
46        state_machine_AFE = GO ;
47        PWM_EN = ON;
48
49        }
50        break;
51
52        case PRECHARGE:
53
54        break;
55
56        case READY:
57
58        break;
59
60        case GO:
61
62        //PI regulators
63        CurrentLoop_d.ref = I_dq_ref.d;
64        CurrentLoop_d.fbk = I_f_dq.d;
65        CurrentLoop_d.ff = V_SOGI_dq.d;
66        CurrentLoop_d.lim_pos = max;
67        CurrentLoop_d.lim_neg = -max;
68        PIReg(&CurrentLoop_d);
69
70        v_prop_d = CurrentLoop_d.out;
71
72        CurrentLoop_q.ref = I_dq_ref.q;
73        CurrentLoop_q.fbk = I_f_dq.q;
74        CurrentLoop_q.ff = 0;
75        CurrentLoop_q.lim_pos = sqrtf((max*max) - (v_prop_d*v_prop_d))
          ;
76        CurrentLoop_q.lim_neg = -CurrentLoop_q.lim_pos;
77        PIReg(&CurrentLoop_q);
```

```
78
79     V_dq_ref.d = CurrentLoop_d.out;
80     V_dq_ref.q = CurrentLoop_q.out;
81
82     V_ab_ref  = dq_alpha_beta(V_dq_ref.d, V_dq_ref.q,
    theta_rad_SOGI);
83         V_abc_ref = alpha_beta_abc(V_ab_ref.alpha, V_ab_ref.beta);
84
85
86      // Zero sequence detection for reasearch of V_common_mode
87
88   if (V_abc_ref.a > V_abc_ref.b)
89   {
90     f32_temp1 = V_abc_ref.a;
91     f32_temp2 = V_abc_ref.b;
92   }
93
94   else
95   {
96     f32_temp1 = V_abc_ref.b;
97     f32_temp2 = V_abc_ref.a;
98   }
99
100  if (f32_temp1 < V_abc_ref.c)
101    f32_ZeroSequence = f32_temp1;
102   else
103  {
104    if (f32_temp2 > V_abc_ref.c)
105      f32_ZeroSequence = f32_temp2;
106    else
107      f32_ZeroSequence = V_abc_ref.c;
108  }
109
```

97

```
110    // Compute the inverter output voltage

111

112    Vref_abc.a = V_abc_ref.a+(0.5f*f32_ZeroSequence);

113    Vref_abc.b = V_abc_ref.b+(0.5f*f32_ZeroSequence);

114    Vref_abc.c = V_abc_ref.c+(0.5f*f32_ZeroSequence);

115

116

117    Duty.a = ( Vref_abc.a  / v_dc ) +0.5f;

118    Duty.b = ( Vref_abc.b / v_dc ) +0.5f;

119    Duty.c = ( Vref_abc.c / v_dc ) +0.5f;

120

121      break;

122

123 }

124

125

126 // OUTPUT

127 OutputSignal(0, 0) = V_abc_ref.a;

128 OutputSignal(0, 1) = V_abc_ref.b;

129 OutputSignal(0, 2) = V_abc_ref.c;

130 OutputSignal(0, 3) = V_ab_ref.alpha;

131 OutputSignal(0, 4) = V_ab_ref.beta;

132 OutputSignal(0, 5) = CurrentLoop_d.out;

133 OutputSignal(0, 6) = CurrentLoop_q.out;

134 OutputSignal(0, 7) = state_machine_AFE;

135 OutputSignal(0, 8) = V_SOGI_dq.d;

136 OutputSignal(0, 9) = V_SOGI_dq.q;

137 OutputSignal(0, 10) = CurrentLoop_d.in;

138 OutputSignal(0, 11) = CurrentLoop_d.out;

139 OutputSignal(0, 12) = CurrentLoop_d.prop;

140 OutputSignal(0, 13) = CurrentLoop_d.intg;

141 OutputSignal(0, 14) = CurrentLoop_d.ff;

142 OutputSignal(0, 15) = CurrentLoop_d.lim_pos;
```

98

```
143 OutputSignal(0, 16) = CurrentLoop_d.lim_neg;
144 OutputSignal(0, 17) = CurrentLoop_d.error;
145 OutputSignal(0, 18) = CurrentLoop_d.lim_int_pos;
146 OutputSignal(0, 19) = CurrentLoop_d.lim_int_neg;
147 OutputSignal(0, 20) = CurrentLoop_d.ref;
148 OutputSignal(0, 21) = CurrentLoop_d.fbk;
149 OutputSignal(0, 22) = I_f_dq.d;
150 OutputSignal(0, 23) = I_f_dq.q;
151 OutputSignal(0, 24) = Duty.a;
152 OutputSignal(0, 25) = Duty.b;
153 OutputSignal(0, 26) = Duty.c;
154 OutputSignal(0, 27) = PWM_EN;
155 OutputSignal(0, 28) = P_ref;
156 OutputSignal(0, 29) = Q_ref;
157 OutputSignal(0, 32) = I_ref_PQ.d;
158 OutputSignal(0, 33) = I_ref_PQ.q;
159 }
```

Listing A.2: C code for control loop

Appendix B

Transformation Matrix

Clarke transformation atrices

This appendix describes the Clarke transformation matrices with all relevant formulas and includes C-scripts for each transformation. We will start with the $abc \rightarrow \alpha\beta$ transformation matrix, followed by the inverse transformation, and finally, the $\alpha\beta \rightarrow dq$ transformation and its inverse.

B.1 $abc \rightarrow \alpha\beta$ Transformation

The Clarke transformation converts three-phase (abc) currents or voltages to two-phase ($\alpha\beta$) components, without modifying their amplitudes. The transformation matrix $\mathbf{A}$ is defined as:

$$\mathbf{A} = \frac{2}{3} \begin{bmatrix} 1 & -\frac{1}{2} & -\frac{1}{2} \\ 0 & \frac{\sqrt{3}}{2} & -\frac{\sqrt{3}}{2} \end{bmatrix}$$

Thus, the transformed components are given by:

$$\begin{bmatrix} I_\alpha \\ I_\beta \end{bmatrix} = \mathbf{A} \begin{bmatrix} I_a \\ I_b \\ I_c \end{bmatrix}$$

C-script for $abc \rightarrow \alpha\beta$ transformation

```
X_alphabeta abc_alpha_beta(double Va, double Vb, double Vc) {
    X_alphabeta result;
    result.alpha = two_over_three * (Va - 0.5 * Vb - 0.5 * Vc);
    result.beta  = one_over_rad2 * (Vb - Vc);

    return result;
}
```

Listing B.1: C-script for $abc \rightarrow \alpha\beta$ Transformation

B.2   Inverse $\alpha\beta \rightarrow abc$ transformation

The inverse Clarke transformation converts $\alpha\beta$ components back to three-phase (abc) currents or voltages. The inverse transformation matrix $\mathbf{A}^{-1}$ is defined as:

$$\mathbf{A}^{-1} = \begin{bmatrix} 1 & 0 \\ -\frac{1}{2} & \frac{\sqrt{3}}{2} \\ -\frac{1}{2} & -\frac{\sqrt{3}}{2} \end{bmatrix}$$

Thus, the inverse transformed components are given by:

101

$$\begin{bmatrix} I_a \\ I_b \\ I_c \end{bmatrix} = \mathbf{A}^{-1} \begin{bmatrix} I_\alpha \\ I_\beta \end{bmatrix}$$

C-script for inverse $\alpha\beta \to abc$ transformation

```
X_abc alpha_beta_abc(double Valpha, double Vbeta) {
    X_abc result;

    result.a = Valpha;
    result.b = ( - 0.5 * Valpha + sqrt3_allover_2 * Vbeta);
    result.c = ( - 0.5 * Valpha - sqrt3_allover_2 * Vbeta);

    return result;
}
```

Listing B.2: C-script for Inverse $\alpha\beta \to abc$ Transformation

B.3 $\alpha\beta \to dq$ transformation

The $\alpha\beta \to dq$ transformation, also known as the Park transformation, rotates the $\alpha\beta$ components to a rotating reference frame (dq). The rotation matrix $\mathbf{R}(\theta)$ is defined as:

$$\mathbf{R}(\theta) = \begin{bmatrix} \cos(\theta) & \sin(\theta) \\ -\sin(\theta) & \cos(\theta) \end{bmatrix}$$

Thus, the transformed components are given by:

$$\begin{bmatrix} I_d \\ I_q \end{bmatrix} = \mathbf{R}(\theta) \begin{bmatrix} I_\alpha \\ I_\beta \end{bmatrix}$$

C-script for $\alpha\beta \to dq$ transformation

```
X_dq alpha_beta_dq(double Valpha, double Vbeta, double theta) {
    X_dq result;
    result.d = (Valpha * cos(theta) + Vbeta * sin(theta));
    result.q = (- Valpha * sin(theta) + Vbeta * cos(theta));

    return result;
}
```

Listing B.3: C-script for $\alpha\beta \to dq$ Transformation

B.4   Inverse $dq \to \alpha\beta$ transformation

The inverse Park transformation converts dq components back to the stationary $\alpha\beta$ reference frame. The inverse rotation matrix $\mathbf{R}^{-1}(\theta)$ is defined as:

$$\mathbf{R}^{-1}(\theta) = \begin{bmatrix} \cos(\theta) & -\sin(\theta) \\ \sin(\theta) & \cos(\theta) \end{bmatrix}$$

Thus, the inverse transformed components are given by:

$$\begin{bmatrix} I_\alpha \\ I_\beta \end{bmatrix} = \mathbf{R}^{-1}(\theta) \begin{bmatrix} I_d \\ I_q \end{bmatrix}$$

C-script for inverse $dq \to \alpha\beta$ transformation

```
X_alphabeta dq_alpha_beta(double Vd, double Vq, double theta) {
    X_alphabeta result;

    result.alpha = Vd * cos(theta) - Vq * sin(theta);
    result.beta  = Vd * sin(theta) + Vq * cos(theta);
```

```
6
7      return result;
8  }
```

Listing B.4: C-script for Inverse $dq \rightarrow \alpha\beta$ Transformation

Bibliography

[1] *Global EV Outlook 2024 – Analysis - IEA — iea.org.* https://www.iea.org/reports/global-ev-outlook-2024. [Accessed 16-05-2024] (cit. on pp. 1–5).

[2] Mathieu Kervyn De Meerendre, Eduardo Prieto-Araujo, Khaled H. Ahmed, Oriol Gomis-Bellmunt, Lie Xu, and Agustí Egea-Àlvarez. «Review of Local Network Impedance Estimation Techniques». In: *IEEE Access* 8 (2020), pp. 213647–213661. DOI: 10.1109/ACCESS.2020.3040099 (cit. on pp. 7, 12, 15).

[3] M. Sumner, B. Palethorpe, and D.W.P. Thomas. «Impedance measurement for improved power quality-Part 1: the measurement technique». In: *IEEE Transactions on Power Delivery* 19.3 (2004), pp. 1442–1448. DOI: 10.1109/TPWRD.2004.829873 (cit. on p. 7).

[4] Marco Tedde and Keyue Smedley. «Anti-Islanding for Three-Phase One-Cycle Control Grid Tied Inverter». In: *IEEE Transactions on Power Electronics* 29.7 (2014), pp. 3330–3345. DOI: 10.1109/TPEL.2013.2278792 (cit. on p. 8).

[5] Mihai Ciobotaru, Remus Teodorescu, Pedro Rodriguez, Adrian Timbus, and Frede Blaabjerg. «Online grid impedance estimation for single-phase grid-connected systems using PQ variations». In: *2007 IEEE Power Electronics Specialists Conference.* 2007, pp. 2306–2312. DOI: 10.1109/PESC.2007.4342370 (cit. on pp. 8, 10, 13).

[6]   Mihai Ciobotaru, Remus Teodorescu, and Frede Blaabjerg. «On-line grid impedance estimation based on harmonic injection for grid-connected PV inverter». In: *2007 IEEE International Symposium on Industrial Electronics.* 2007, pp. 2437–2442. DOI: `10.1109/ISIE.2007.4374989` (cit. on p. 9).

[7]   Abdelhady Ghanem, Mohamed Rashed, Mark Sumner, M. A. El-sayes, and I. I. I. Mansy. «Grid impedance estimation for islanding detection and adaptive control of converters». In: *8th IET International Conference on Power Electronics, Machines and Drives (PEMD 2016).* 2016, pp. 1–6. DOI: `10.1049/cp.2016.0205` (cit. on p. 13).

[8]   Bahman Alinezhad and Hossein Kazemi Karegar. «On-Line Thévenin Impedance Estimation Based on PMU Data and Phase Drift Correction». In: *IEEE Transactions on Smart Grid* 9.2 (2018), pp. 1033–1042. DOI: `10.1109/TSG.2016.2574765` (cit. on p. 13).

[9]   Sandro Corsi and Glauco N. Taranto. «A Real-Time Voltage Instability Identification Algorithm Based on Local Phasor Measurements». In: *IEEE Transactions on Power Systems* 23.3 (2008), pp. 1271–1279. DOI: `10.1109/TPWRS.2008.922586` (cit. on p. 13).

[10] Nils Hoffmann and Friedrich Wilhelm Fuchs. «Minimal Invasive Equivalent Grid Impedance Estimation in Inductive–Resistive Power Networks Using Extended Kalman Filter». In: *IEEE Transactions on Power Electronics* 29.2 (2014), pp. 631–641. DOI: `10.1109/TPEL.2013.2259507` (cit. on p. 13).

[11] Pablo García, Mark Sumner, Ángel Navarro-Rodríguez, Juan M. Guerrero, and Jorge García. «Observer-Based Pulsed Signal Injection for Grid Impedance Estimation in Three-Phase Systems». In: *IEEE Transactions on Industrial Electronics* 65.10 (2018), pp. 7888–7899. DOI: `10.1109/TIE.2018.2801784` (cit. on p. 15).

[12] Santiago Cobreces, Emilio J. Bueno, Daniel Pizarro, Francisco J. Rodriguez, and Francisco Huerta. «Grid Impedance Monitoring System for Distributed Power Generation Electronic Interfaces». In: *IEEE Transactions on Instrumentation and Measurement* 58.9 (2009), pp. 3112–3121. DOI: `10.1109/TIM.2009.2016883` (cit. on p. 15).

[13] Davide Cittanti, Fabio Mandrile, Matteo Gregorio, and Radu Iustin Bojoi. «Design Space Optimization of a Three-Phase LCL Filter for Electric Vehicle Ultra-Fast Battery Charging». In: *Energies* (2021). URL: `https://api.semanticscholar.org/CorpusID:233881369` (cit. on pp. 17, 21).

[14] «IEEE Standard for Harmonic Control in Electric Power Systems». In: *IEEE Std 519-2022 (Revision of IEEE Std 519-2014)* (2022), pp. 1–31. DOI: `10.1109/IEEESTD.2022.9848440` (cit. on p. 20).

[15] Vincenzo Mallemaci Radu Bojoi Fabio Mandrile. *Power Electronics for Grid applications.* . [Accessed 05-06-2024]. 2023 (cit. on pp. 21, 23, 24, 26–28, 31).

[16] Radu Bojoi. *Power Electronics for e-mobility.* . [Accessed 05-06-2024]. 2021 (cit. on pp. 32, 34).

[17] Radu Iustin Bojoi, G. Griva, Valeriu Bostan, Maurizio Guerriero, Francesco Farina, and Francesco Profumo. «Current control strategy for power conditioners using sinusoidal signal integrators in synchronous reference frame». In: *IEEE Transactions on Power Electronics* 20 (2005), pp. 1402–1412. URL: `https://api.semanticscholar.org/CorpusID:41613330` (cit. on p. 40).

[18] Fabio Mandrile. *SSI Filter Exact Discretisation.* `FabioMandrile.SSIFilter ExactDiscretisation,August2018.`. [Accessed 05-06-2024] (cit. on p. 40).

[19] Hesam Khazraj, F. Faria da Silva, and Claus Leth Bak. «An improved current controller to ensure the robust performance of grid-connected converters under weak grid Conditions». In: *2016 IEEE 16th International Conference*

on Environment and Electrical Engineering (EEEIC). 2016, pp. 1–6. DOI: `10.1109/EEEIC.2016.7555633` (cit. on p. 45).

[20] Adrian V. Timbus, Pedro Rodriguez, Remus Teodorescu, and Mihai Ciobotaru. «Line Impedance Estimation Using Active and Reactive Power Variations». In: *2007 IEEE Power Electronics Specialists Conference*. 2007, pp. 1273–1279. DOI: `10.1109/PESC.2007.4342176` (cit. on pp. 45, 54).

[21] Adrian V. Timbus, Pedro Rodriguez, Remus Teodorescu, and Mihai Ciobotaru. «Line Impedance Estimation Using Active and Reactive Power Variations». In: *2007 IEEE Power Electronics Specialists Conference*. 2007, pp. 1273–1279. DOI: `10.1109/PESC.2007.4342176` (cit. on p. 45).

[22] Jingyang Fang, Han Deng, and Stefan M. Goetz. «Grid Impedance Estimation Through Grid-Forming Power Converters». In: *IEEE Transactions on Power Electronics* 36.2 (2021), pp. 2094–2104. DOI: `10.1109/TPEL.2020.3010874` (cit. on p. 45).

[23] Roberto A. Fantino, Claudio A. Busada, and Jorge A. Solsona. «Grid Impedance Estimation by Measuring Only the Current Injected to the Grid by a VSI With *LCL* Filter». In: *IEEE Transactions on Industrial Electronics* 68.3 (2021), pp. 1841–1850. DOI: `10.1109/TIE.2020.2973910` (cit. on p. 45).

[24] L. Asiminoaei, R. Teodorescu, F. Blaabjerg, and U. Borup. «Implementation and test of an online embedded grid impedance estimation technique for PV inverters». In: *IEEE Transactions on Industrial Electronics* 52.4 (2005), pp. 1136–1144. DOI: `10.1109/TIE.2005.851604` (cit. on pp. 56, 63, 72, 79).

[25] L. Asiminoaei, R. Teodorescu, F. Blaabjerg, and U. Borup. «Implementation and test of an online embedded grid impedance estimation technique for PV inverters». In: *IEEE Transactions on Industrial Electronics* 52.4 (2005), pp. 1136–1144. DOI: `10.1109/TIE.2005.851604` (cit. on pp. 56, 57).

108

[26] R. Parthiban, T. Nivetha, and B. Umamaheswari. «Harmonic injection technique-based grid impedance estimation for an LCL-filtered grid connected inverter - an investigation». In: *International Journal of Power Electronics* (2019). URL: https://api.semanticscholar.org/CorpusID:117186595 (cit. on p. 56).

[27] Mihai Ciobotaru, Remus Teodorescu, and Frede Blaabjerg. «On-line grid impedance estimation based on harmonic injection for grid-connected PV inverter». In: *2007 IEEE International Symposium on Industrial Electronics.* 2007, pp. 2437–2442. DOI: 10.1109/ISIE.2007.4374989 (cit. on p. 56).